

**Attachment B**  
**DOE team's Task 2D report**

**DECOVALEX III Task 2D report**

Thermal-hydrological-chemical model of  
the Drift Scale Test

Eric Sonnenthal and Nicolas Spycher

Lawrence Berkely national Laboratory  
California, USA

2004

## B1. Introduction

The Drift Scale Test (DST) is the second underground thermal test to be carried out in the Exploratory Studies Facility (ESF) at Yucca Mountain, Nevada. The purpose of the test is to evaluate the coupled thermal, hydrological, chemical, and mechanical processes that take place in unsaturated fractured tuff over a range of temperatures (approximately 25°C to 200°C). Details regarding the DST layout, borehole orientations, operation of the test, and measurements performed are discussed in Section 6.3 of the *Thermal Testing Measurements Report* (BSC 2002a) and in *Drift Scale Test As-Built Report* (CRWMS M&O 1998). Information on these aspects of the DST is not repeated in this report unless directly related to the geochemical data collected and used for model validation.

In brief, the DST consists of an approximately 50 m long drift that is 5 m in diameter. Nine electrical floor canister heaters were placed in this drift (the Heated Drift) to simulate nuclear-waste-bearing containers. Electrical heaters were also placed in a series of horizontal boreholes (wing heaters) drilled perpendicular outward from the central axis of the Heated Drift. These heaters were emplaced to simulate the effect of adjacent emplacement drifts. The DST heaters were activated on December 3, 1997, with a planned period of 4 years of heating, followed by 4 years of cooling. After just over 4 years, the heaters were switched off on January 14, 2002, and since that time the test area has been slowly cooling.

This report describes the conceptual and numerical model for evaluating thermal-hydrological-chemical (THC) processes in the DST, and presents comparisons of simulation results to geochemical measurements performed on gas, water, and mineral samples collected from the DST. The model is not calibrated to geochemical data collected from the DST. Calibrated drift-scale hydrological properties and thermal properties are used as inputs, which are based on Yucca Mountain site data and not data specific to the DST. Some minor modifications were made to the thermodynamic data to better approach equilibrium of the ambient-system pore-water chemistry. Model adjustments specific to the DST are made only to the connectivity of the Heated Drift to the Access Drift, in order to capture (approximately) the heat losses through the bulkhead separating these tunnels and the 2-D nature of the numerical mesh used.

Because of the relatively short duration of the DST, it was not expected that significant changes to permeability would result from mineral precipitation and/or dissolution. The rate of such changes, though, is closely tied to the changes in water chemistry that are directly tied to mineral reaction rates and boiling processes. Therefore, the purpose of the analysis and modeling of the DST is to capture the chemical changes in water and gas as well as to document observed mineralogical changes. Although mechanical processes were certainly active during the DST, measured changes in air permeability were typically less than one order of magnitude (BSC, 2002a). Air permeability reductions could also be attributed to increases in fracture liquid saturation in the condensation zones. In addition, variations in fracture permeability are at least a few orders of magnitude around the DST and therefore smaller mechanical effects would not have a major effect on changes in water and gas chemistry resulting from coupled THC processes.

The first predictive model for THC processes in the DST was begun just prior to the initiation of heating in late 1997 with the final predictive report completed several months after the test had begun (Sonnenthal et al. 1998; Xu et al., 2001). The 2-D numerical grid, thermal and hydrological properties for the THC model were based on the original TH model developed for the DST (Birkholzer and Tsang, 1997; 1998).

Numerous updates to the DST THC Model have been made to account for additional chemical and mineralogical components, as well as revised thermal, chemical, and hydrological properties, and improved process model and code implementations (i.e., the TOUGHREACT code discussed in Section 3). Discussion of these revisions and comparison to data collected during the heating phase of the DST are presented in Sonnenthal et al. (1999), Sonnenthal and Spycher (2000, 2001) and Spycher et al. (2003).

The most important improvements in the DST THC Model since the original predictive report came from the collection and analysis of initial pore water data from the rock adjacent to the test block, from revisions in the kinetic and thermodynamic data, and improvements in the treatment of mineral precipitation at the boiling front. Analyses done for the predictive report relied on an average composition of pore water from the top and base of the Topopah Spring Tuff, which turned out to be more somewhat more dilute than the pore water collected later from the rock.

## **B2. Conceptual model for THC processes**

The evolution of the chemical regime in the unsaturated zone surrounding a heat source is closely related to the spatial distribution of temperature and the transport of water and vapor. An important aspect of the unsaturated fractured tuff at Yucca Mountain is that the highly permeable fractures are nearly dry, whereas the low permeability and porosity rock matrix has a water saturation of about 90 percent. Thus, heating of the rock induces boiling of the matrix pore water, transport of water vapor into fractures, and condensation along fracture walls. The numerical model for reaction-transport processes in the fractured welded tuffs must account for the different rates of transport in fractures, compared to a much less permeable rock matrix. Transport rates greater than the rate of equilibration via diffusion leads to disequilibrium between waters in fractures and matrix. Because the system is unsaturated, and undergoes boiling, the transport of gaseous species, especially CO<sub>2</sub>, is an important consideration. The model must also capture the differences in initial mineralogy in fractures and matrix and their evolution.

In order to handle separate yet interacting processes in fractures and matrix, the dual permeability method has been adopted, such that each grid block is divided into matrix and fracture continua, characterized by their own pressure, temperature, liquid saturation, water and gas chemistry, and mineralogy. In the dual-permeability model, the fracture continuum is considered as co-located but interacting with the matrix continuum, in terms of the flow of heat, water, and vapor through advection, diffusion, and conduction (for heat). The aqueous and gaseous species are transported via advection and molecular diffusion between the fractures and matrix. Each continuum has its own well-defined initial physical and chemical properties.

## **B3. Mathematical model**

Simulations of THC processes include coupling between heat, water, and vapor flow; aqueous and gaseous species transport; kinetic and equilibrium mineral-water reactions; and feedback of mineral precipitation/dissolution on porosity, permeability, and capillary pressure. This section describes the mathematical formulations in TOUGHREACT V3.0 (BSC 2002b) used to describe these coupled phenomena.

Equations for heat, liquid and gas flow, aqueous and gaseous species transport, and chemical reactions are summarized in Xu and Pruess (2001, 1998) and Xu et al. (1998). Flow and reaction/transport equations are solved sequentially (e.g., Steefel and Lasaga 1994). This section describes the mathematical relations important to thermodynamic and kinetic aspects of mineral-water-gas reactions that are unique to solving the coupled THC processes.

### B3.1 Geochemical model

The geochemical module incorporated in TOUGHREACT V3.0 simultaneously solves a set of chemical mass-action, kinetic-rate expressions for mineral dissolution/precipitation, and mass-balance equations. This provides the extent of reaction and mass transfer between a set of given aqueous species, minerals, and gases at each grid block of the flow model. Equations for mineral-chemical equilibrium, kinetic rates, and permeability/porosity changes are given further below.

The setup of mass-action and mass-balance equations in TOUGHREACT is similar to the formulation implemented in Reed (1982). Additional provisions are made for mineral dissolution and precipitation under kinetic constraints and a volume-dependent formulation for gas equilibrium, as described below. The chemical system is described in terms of primary aqueous species (the independent variables). Minerals, gases, and secondary aqueous species are defined in terms of reactions involving only the primary species. It has been shown that if the diffusivities of all aqueous species are equal, only the transport of primary species (in terms of total dissolved concentrations) needs to be considered to solve the entire reactive flow/transport problem (Steefel and Lasaga 1994).

The system of nonlinear equations describing chemical mass-balance, mass-action, and kinetic-rate expressions is solved by a Newton-Raphson iterative procedure. In TOUGHREACT, activity coefficients of charged species and the activity of water are calculated with the method of Helgeson et al. (1981). Using this method, activities of water and activity coefficients of electrolytes typical of natural systems (NaCl, CaCl<sub>2</sub>, Mg<sub>2</sub>SO<sub>4</sub>, Ca<sub>2</sub>SO<sub>4</sub>) were fairly well reproduced up to ionic strengths of 6 molal. Activity coefficients of selected neutral species are calculated using salting-out coefficients as described in Langmuir (1997).

Equilibration with mineral phases is computed by adding a mass-action equation, for each saturated mineral, into the system of nonlinear equations as follows:

$$\log(K_i) = \log(Q_i) \tag{B1}$$

where  $K_i$  denotes the equilibrium constant and  $Q_i$  the product of the ion activities in the reaction that expresses mineral  $i$  in terms of the primary aqueous species. A term representing the amount of primary aqueous species consumed or produced by equilibration of minerals is added to the mass-balance equation for each primary species involved in mineral reactions, and this term is solved simultaneously with the concentrations of all primary species. Minerals thus dissolve if  $\log(Q_i/K_i) < 0$  and precipitate if  $\log(Q_i/K_i) > 0$ . A “supersaturation gap” can be specified, by which the mineral is not allowed to precipitate if  $\log(Q_i/K_i)$  is greater than zero but less than a specified “gap” value (a positive number). This gap can be set to decrease exponentially with increasing temperature.

Gas species, such as CO<sub>2</sub>, are treated as ideal mixtures of gases in equilibrium with the aqueous solution. A mass-action equation is added to the system of simultaneous equations for each saturated gas present—except for H<sub>2</sub>O vapor and air, which are handled separately through the flow module in TOUGHREACT. The gas mass-action equation takes the form:

$$\log(K_i) = \log(Q_i) - \log(P_i) \quad (\text{B2})$$

where  $P_i$  is the partial pressure of gaseous species  $i$ .  $P_i$  is first calculated from the advective-diffusive gas transport equation in TOUGHREACT. Then  $P_i$  is replaced with the ideal gas law,

$$P_i = \frac{n_i RT}{V_g} \quad (\text{B3})$$

where  $n_i$  denotes the number of moles of gas species  $i$ ,  $R$  is the gas constant,  $T$  is the absolute temperature, and  $V_g$  is the gas total volume. By expressing  $V_g$  in terms of the gas saturation  $S_g$ , the porosity of the medium  $\phi$ , and the volume of each grid block in the flow model  $V_{block}$ , Equation 3 is rewritten as:

$$P_i = \frac{n_i RT}{V_{block} \phi S_g} \quad (\text{B4})$$

The gas saturation is computed in the flow module of TOUGHREACT (reflecting H<sub>2</sub>O and air partial pressures computed in this module). The amount of trace gas species ( $n_i/V_{block}$ ) is then obtained by substitution of Equation B4 into Equation B2 and solving together with the concentrations of all primary species.

The partial pressures of trace gas species are not fed back to the multiphase flow module of TOUGHREACT for solving the water and gas flow equations. Therefore, this method should only be applied to gases (excluding H<sub>2</sub>O and air) with partial pressures significantly lower than the total gas pressure. No absolute cutoff exists at which this approximation breaks down, and therefore it is validated by comparison to DST-measured CO<sub>2</sub> concentrations. For cases where the partial pressures of a trace gas become closer to the total pressure, chemical equilibrium with the aqueous phase is computed correctly, but the gas pressure will be underestimated in the mass-balance equation solved for gas flow. Because CO<sub>2</sub> concentrations encountered in the DST and model simulations are generally less than a few percent, and rarely over 10%, this model for the gas species is a reasonable approximation for this particular system.

### B3.2 Kinetic rate laws

Rates of mineral dissolution and precipitation close to equilibrium can be described via a relationship of the rate to the saturation index ( $Q/K$ ), as follows (Steeffel and Lasaga 1994):

$$Rate(\text{mol } s^{-1} \text{kg}_{\text{water}}^{-1}) = \text{sgn} \left[ \log \left( \frac{Q}{K} \right) \right] k A \prod_i a_i^p \left[ \left( \frac{Q}{K} \right)^m - 1 \right]^n \quad (\text{B5})$$

where  $a_i$  is the activity of each inhibiting or catalyzing species, and  $p$  is an empirically determined exponent and the variable  $A$  is the reactive surface area expressed in units of  $m_{\text{mineral}}^2 / kg_{\text{water}}$ . The rate constant  $k$  (in  $\text{mol m}^{-2} \text{s}^{-1}$ ) is given as (Steefel and Lasaga 1994):

$$k = k_0 \exp \left[ \frac{-E_a}{R} \left( \frac{1}{T} - \frac{1}{298.15} \right) \right] \quad (\text{B6})$$

where the temperature dependence of reaction rate is related to the activation energy ( $E_a$ ) in units of kJ/mol and  $T$  is the temperature in Kelvin units. Following Steefel and Lasaga (1994), by neglecting the effect of pH or other aqueous species activities on reaction rates, we set  $p=0$  for each species so that the product  $\prod_i a_i^p = 1$  has been

eliminated from Equation B5. The ratio of the species activity product ( $Q$ ) and the equilibrium constant ( $K$ ) describes the extent to which a mineral is in disequilibrium with a given solution composition. For  $Q/K$  equal to one, the mineral is at equilibrium, and thus the net rate of reaction becomes zero. For  $Q/K$  greater than one, the mineral is oversaturated and thus the rate becomes negative. The expression “ $\text{sgn} [\log(Q/K)]$ ” ensures that the correct sign is enforced when the exponents  $m$  and  $n$  are not equal to one. The variable  $A$  is the reactive surface area expressed in units of  $m_{\text{mineral}}^2 / kg_{\text{water}}$ . In the case of ideal solutions, the saturation index of the solid solution is calculated as the sum of the saturation indices of the individual end members, and the reaction rate of the solid solution is calculated.

Carroll et al. (1998) noted that the calculated rates of amorphous silica precipitation, based on Rimstidt and Barnes (1980), are about three orders of magnitude lower than those observed in geothermal systems. Carroll et al. (1998) presented experimental data on amorphous silica precipitation for more complex geothermal fluids at higher degrees of supersaturation, and also for a near-saturation simple fluid chemistry. Under far from equilibrium conditions, the rate law for amorphous silica precipitation has been expressed as (Carroll et al. 1998):

$$\text{Rate}(\text{mol s}^{-1} \text{kg}_{\text{water}}^{-1}) = kA \left( \frac{Q}{K} \right)^m \quad (\text{B7})$$

This rate does not tend to zero as  $Q/K$  goes to one, and therefore a modification was made to this law so that it tends to zero as  $Q/K$  approaches one, as follows:

$$\text{Rate}(\text{mol s}^{-1} \text{kg}_{\text{water}}^{-1}) = kA \left[ \left( \frac{Q}{K} \right)^m - \frac{1}{\left( \frac{Q}{K} \right)^{2m}} \right] \quad (\text{B8})$$

Over a finite time step ( $\Delta t$ ), the change in the concentration of each primary species  $j$  on account of mineral precipitation or dissolution under kinetic constraints is computed from the sum of the rates,  $r_i$ , of all  $j$ -containing minerals  $i$  as follows:

$$\Delta C_j = -\sum r_i \nu_{ij} \Delta t \quad (\text{B9})$$

where  $\nu_{ij}$  is the stoichiometric coefficient of component  $j$  in mineral  $i$ . These concentration changes are incorporated into the mass-balance equation of each primary species involved in mineral reactions, using Equations B5 through B7, and solved simultaneously with the concentrations of all primary species.

### B3.3 Reactive surface areas for mineral-water reactions

#### B3.3.1 Fracture mineral reactive surface areas

Reactive surface areas of minerals on fracture walls were calculated from the fracture-matrix interface area/volume ratio, the fracture porosity, and the derived mineral volume fractions. The fracture-matrix interface areas and fracture porosities for each unit were taken from the drift-scale calibrated hydrological property sets. These areas were based on the fracture densities, fracture porosities, and mean fracture diameter. The wall of the fracture is treated as a surface covered by mineral grains having the form of uniform hemispheres. The grain diameter and spatial density are not included in this calculation, so that the area is actually only marginally greater than the fracture geometric surface area. An alternative method to approximating the surface area in excess of the geometric area would be to include a roughness factor. The geometric surface area of the fracture wall can be approximated by:

$$A_r = \frac{\pi A_{f-m}}{2\phi_{f-m}} \quad (\text{B10})$$

where,  $A_r$  is the reactive surface area ( $\text{m}^2 / \text{m}^3_{\text{fracture medium}}$ ),  $A_{f-m}$  is the fracture-matrix interface area/volume ratio ( $\text{m}^2_{\text{fracture}} / \text{m}^3_{\text{fracture+matrix}}$  volume), and  $\phi_{f-m}$  is the fracture porosity of the rock.  $A_{f-m}$  is the surface area used as input to the model simulations as an approximation of the reactive surface area. This model for the fracture surface area considers that the area is approximately equivalent to the mineral volume fraction. A further modification relates the 3-D cross-sectional area to the 2-D surface area in the fracture, yielding a factor of 3/2, i.e., an increase of 50% in the reactive surface area.

The reactive surface area of each mineral (in units of  $\text{m}^2_{\text{mineral}} / \text{kg}_{\text{water}}$ ) used in Equations 5 and 8 is then given by:

$$A_i (\text{m}^2 / \text{kg}_{\text{water}}) = \frac{A_r f_i}{\rho_w \phi_f} \quad (\text{B11})$$

where  $f_i$  is the volume fraction of the mineral in the mineral assemblage,  $\rho_w$  is the density of water (taken as a constant  $1,000 \text{ kg/m}^3$ ), and  $\phi_f$  is the porosity of the fracture medium, as opposed to the fracture porosity of the rock. This is the surface area/water mass ratio for a mineral in a liquid-saturated system. Volume fractions of minerals are tabulated in Spycher et al. (2003).

To provide the correct rock/water ratio in an unsaturated system, the form of this surface area can be written as:

$$A_i (\text{m}^2 / \text{kg}_{\text{water}}) = \frac{A_r f_i}{\rho_w \phi_f S_w} \quad (\text{B12})$$

where  $S_w$  is the water saturation. However, as  $S_w$  goes to zero, the reactive surface area would tend to infinity. Clearly, at a very low liquid saturation, the surface area of the rock contacted by water is likely much smaller than the total area.

Two methods have been implemented to address this phenomenon. The first method considers that the surface area contacted by water diminishes proportionately to the saturation. This yields the saturated surface area given by Equation 10. The second method employs the active-fracture-model concept (Liu et al. 1998) modified to consider water-rock reactions taking place below the residual saturation. The form of the active fracture parameter for reaction is then given by the following set of equations:

$$S_{ar} = (S_w - S_m) / (1 - S_m) \quad (\text{B13})$$

$$a_{fmr} = S_{ar}^{(1+\gamma)} \quad (\text{B14})$$

where  $S_m$  is the minimum liquid saturation for which water-rock reactions are considered and  $S_{ar}$  is the effective saturation available for reaction. The active fracture parameter,  $a_{fmr}$ , is obtained from the calibrated hydrological property set. The factor that reduces the surface area contacted by the water phase is given by  $a_{fmr}$ . In all simulations  $S_m$  is set to the very small saturation of  $1 \times 10^{-4}$  or  $1 \times 10^{-5}$  to ensure that reactions take place until virtually no water is left (e.g., during dry-out via ventilation or heating). Finally, the reactive surface area, using this modified form of the active fracture model, is given by:

$$A_i (\text{m}^2 / \text{kg}_{\text{water}}) = \frac{A_r a_{fmr}}{\rho_w \phi_f S_w} \quad (\text{B15})$$

The surface area calculated in this way is applicable only to reactions taking place in the fracture medium and is used directly in Equations 5 and 8. Note that this area is not comparable to the input surface areas that are listed in Spycher et al. (2003).

In the dual permeability method, the porosity of the fracture medium can be taken as 1.0; however, for modeling of mineral dissolution and precipitation, there would then be no rock to dissolve. Because the dissolution rates of many minerals are quite slow at temperatures below 100°C, only a small volume of rock adjoining the open space of the fracture needs to be considered as the starting rock fraction.

### B3.3.2 Matrix mineral reactive surface areas

Mineral surface areas in the rock matrix are given in Spycher et al. (2003). These values were estimated using the geometric area of a cubic array of truncated spheres that make up the framework of the rock. Clay minerals are considered as coatings of plate-like grains. The mineral surface areas of framework grains (truncated spheres) in contact with the open pore space are calculated using an initial grain diameter, followed by successive truncation of the grains in the vertical direction until the porosity of this system is close to the measured porosity of the rock. In the welded tuff, crystals are

often tightly intergrown with little or no pore space within the aggregate. Thus, a check is made so that the resultant mean pore throat size and spacing yields a permeability (from a modified Hagen-Poiseuille relation (Ehrlich et al. 1991) that is relatively close to the measured saturated permeability.

The grains forming the framework of this rock are considered to be the primary high-temperature phases of the tuff (i.e., quartz, cristobalite, tridymite, and feldspars). The abundances of secondary phases (i.e., those that formed as alteration products or low-temperature coatings on the primary assemblage), such as clay minerals, are used to reduce the free surface area of the framework grains. The surface areas of the secondary phases are approximated using a tabular morphology.

### **B3.4 Effects of mineral precipitation/dissolution on hydrological properties**

#### **B3.4.1 Porosity changes**

The porosity of the medium (fracture or matrix) is given by

$$\phi = 1 - \sum_{m=1}^{nm} fr_m - fr_u \quad (\text{B16})$$

where  $nm$  is the number of minerals,  $fr_m$  is the volume fraction of mineral  $m$  in the rock ( $V_{\text{mineral}}/V_{\text{medium}}$ , including porosity), and  $fr_u$  is the volume fraction of nonreactive rock. As the  $fr_m$  of each mineral changes, the porosity is recalculated at each time step.

#### **B3.4.2 Fracture permeability changes**

In many experimental and natural systems, permeability reductions to values near zero occur at porosities significantly greater than zero. This generally is the result of mineral precipitation preferentially closing the narrower interconnecting apertures. The hydraulic aperture, as calculated from the fracture spacing and permeability (as determined through air-permeability measurements) using a cubic law relation, is a closer measure of the smaller apertures in the flow system. The initial hydraulic aperture  $b_{0,h}$  (m) is calculated using the following cubic law relation:

$$b_{0,h} = [12k_0s]^{1/3} \quad (\text{B17})$$

where  $k_0$  is the initial fracture permeability ( $\text{m}^2$ ) and  $s$  is the fracture spacing (m) for a single fracture set. The permeability ( $k$ ) resulting from a change in the hydraulic aperture is given by

$$k' = \frac{(b_{0,h} + \Delta b)^3}{12s} \quad (\text{B18})$$

where  $\Delta b$  is the aperture change resulting from mineral precipitation/dissolution. The aperture change resulting from a calculated volume change can be approximated by

assuming precipitation of a uniform layer over the entire geometric surface area of the fracture, assuming also that this area (as well as the fracture spacing) remains constant. The initial aperture available for precipitation ( $b_g$ , the geometric, rather than the hydraulic, aperture) can be calculated from the ratio of the initial fracture porosity ( $\phi_{f,0}$ ) to the fracture surface area ( $A_f$ ), as follows:

$$b_g = \phi_{f,0} / A_f \quad (\text{B19})$$

For a dual-permeability model, changes in the fracture porosity are calculated based on the porosity of the fracture medium, so that  $\Delta b$  can be approximated by

$$\Delta b = \frac{(\phi'_{fm} - \phi_{fm,0})}{\phi_{fm,0}} b_g \quad (\text{B20})$$

The parameters  $b_g$  and  $s$  must be supplied in the input file.

### B3.4.3 Matrix permeability changes

Matrix permeability changes are calculated from changes in porosity using ratios of permeabilities calculated from the Carmen-Kozeny relation (Bear 1988; replacing  $n$  by  $\phi$ ), and neglecting changes in grain size, tortuosity, and specific surface area as follows:

$$k = k_i \frac{(1 - \phi_i)^2}{(1 - \phi)^2} \left( \frac{\phi}{\phi_i} \right)^3 \quad (\text{B21})$$

### B3.4.4 Effects of permeability and porosity changes on capillary pressures

Changing permeability and porosity also results in changes in the unsaturated flow properties of the rock. These effects are treated by modifying the calculated capillary pressure ( $Pc$ ) using the Leverett scaling relation (Slider 1976) to obtain a scaled  $Pc'$  as follows:

$$Pc' = Pc \sqrt{\frac{k_i \phi}{k \phi_i}} \quad (\text{B22})$$

Simulations performed with TOUGHREACT have the maximum value of  $Pc'$  (in Eq. B22) limited by the cutoff prescribed in the input file.

## B3.5 Mineral precipitation in dry grid blocks

In certain cases of evaporation or boiling, a grid block may experience an influx of water that evaporates completely during the solution of the flow equations. After the flow equations are solved, TOUGHREACT solves the transport equations followed by the speciation and reaction equations. The speciation and reaction equations require that

the grid block is “wet,”—that is, the liquid saturation is greater than zero (or a small value). Because of the lack of water in the grid block, a method was developed for storing residual aqueous species in a solid “salt” assemblage.

Typically upon boiling or evaporation, once the ionic strength of the aqueous fluid reaches an input upper limit of 4, or if the liquid saturation drops below an input lower limit of  $10^{-4}$  to  $10^{-5}$ , the aqueous phase is treated as non-reactive and is not concentrated further. This ensures that the calculated ionic strength remains within the range of applicability of activity coefficient models. Solid phases are formed during dryout as described below.

The amount of solute “stored” is simply the product of the concentration in the upstream grid block and the flux of water into the grid block that dries out. Also, any water that is initially present in the grid block, and dries out, gives rise to some solute mass that is transformed into solid phases. For these cases, the mass of each primary solute species is saved and may be assigned to minerals in a prescribed order in the chemical input file. This approximation is performed so that solute mass loss is minimized and most of the solute mass can be accounted for in a solid mineral phase.

In the simulations presented in this report, for the specific cases when water flows into grid blocks that dry out in the flow calculation (by boiling or evaporation), the following solid phases are formed, stoichiometrically, and in the following order: silica, calcite, gypsum, hematite, fluorite,  $\text{NaNO}_3$ ,  $\text{K}_2\text{SO}_4$ ,  $\text{Na}_2\text{SO}_4$ ,  $\text{MgSO}_4$ , halite, and sylvite. The order is predetermined (i.e., nitrates are formed before chlorides) to ensure nitrate mass is not lost in cases where insufficient sodium remains to form  $\text{NaNO}_3$  (in the absence of other nitrate salts that could have formed). The goal, here, is not to model evaporation accurately but to save as much mass of the dissolved constituents as possible for grid blocks that completely dry out. Upon rewetting, the salt minerals are assumed to dissolve kinetically with a relatively fast rate constant (set here at  $10^{-6}$  mol/m<sup>2</sup>/s) and a dissolution rate limited by their solubility.

### B3.6 Transport parameters

Diffusion coefficients of all aqueous species are set to the same value (the value for the chloride anion). This is justified because the tracer diffusion coefficients of aqueous species differ by at most about one order of magnitude, with many differing by less than a factor of 2 (Lasaga 1998). The strong effects of water-rock interaction, boiling condensation, and rapid fracture drainage in the DST overwhelm effects of aqueous species diffusion.

Diffusion coefficients for gases are calculated. In the gas phase,  $\text{CO}_2$  is the only transported reactive species (other than  $\text{H}_2\text{O}$  vapor). For an ideal gas, the tracer diffusion coefficient of a gaseous species can be expressed as a function of temperature and pressure in the following form (Lasaga 1998):

$$D = \frac{RT}{3\sqrt{2}\pi P N_A d_m^2} \sqrt{\frac{8RT}{\pi M}} \quad (\text{B23})$$

where  $D$  = diffusion coefficient (m<sup>2</sup>/s),  $R$  = gas constant (8.31451 m<sup>2</sup> kg s<sup>-2</sup> mol<sup>-1</sup> K<sup>-1</sup>),  $T$  = temperature in Kelvin units,  $P$  = pressure (kg m<sup>-1</sup> s<sup>-2</sup>),  $N_A$  = Avogadro's number (6.0221367 x 10<sup>23</sup> mol<sup>-1</sup>),  $d_m$  = molecular diameter (m) and  $M$  = molecular weight (kg/mol), respectively.

The CO<sub>2</sub> diffusion coefficient is calculated using input values of  $d_m$  and  $M$  (given in the thermodynamic data table).

## B4. Drift Scale Test THC model

### B4.1 Drift Scale Test 2-D numerical grid

The two-dimensional dual-permeability numerical grid for the DST represents a vertical cross section through the Heated Drift at a distance approximately 30 m from the bulkhead, separating the Heated Drift from the Access Drift (Figure B1a). The mesh consists of 4,490 grid blocks, including fracture and matrix (Figure 1a and 1b). The top boundary is approximately 99 m above the drift center, with the bottom boundary at approximately 157 m below the center. The DST includes a plane of linear wing heaters on each side of the drift that are given small grid blocks in the model. Small grid blocks are also employed adjacent to the wing heaters and drift wall to capture the strong gradients in temperature and liquid saturation in these regions (Figure B1b). Radial mesh blocks in the drift interior were removed from the original mesh and replaced near the drift base by Cartesian grid blocks to represent the concrete invert (Figure B1b). The Heated Drift grid block is connected directly to the Heater Test Alcove grid block. The connection area and distance were adjusted so that heat loss from the drift resulted in roughly similar crown temperatures to the maximum observed values. This was done to simulate heat and mass losses through the bulkhead, instead of reducing power by a set factor. In the approximate location of the observation drift, the grid block volumes were increased to a large value to represent connection to the atmosphere. The distances from the drift center grid block and the connecting elements were modified to represent the true distance, so that heat could be applied to the drift center to approximate the effect of the electrical canister heaters. The locations of the hydrology boreholes, sampling intervals (numbered) and temperature sensors are shown in Figure B2.

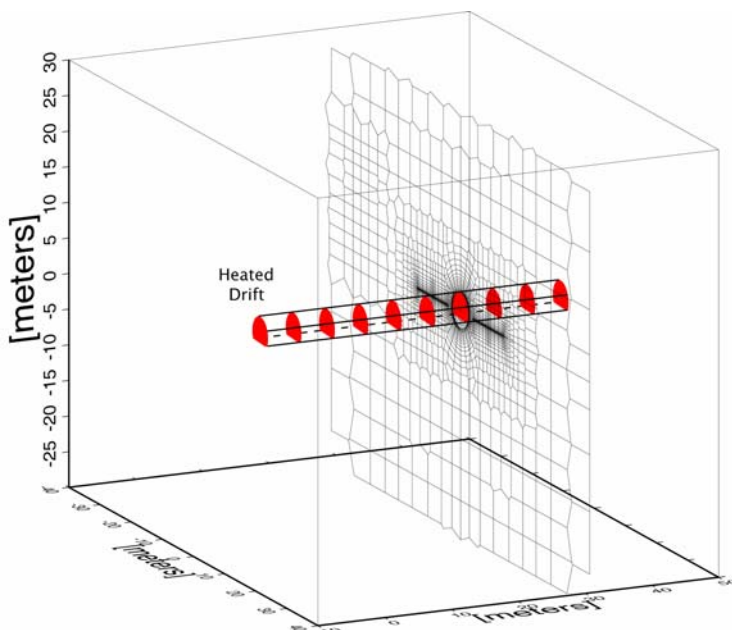


*Figure B1a. Three-dimensional schematic diagram of the DST showing perspective view of 2-D numerical mesh for DST THC model simulations (mesh extends in all directions from area shown).*

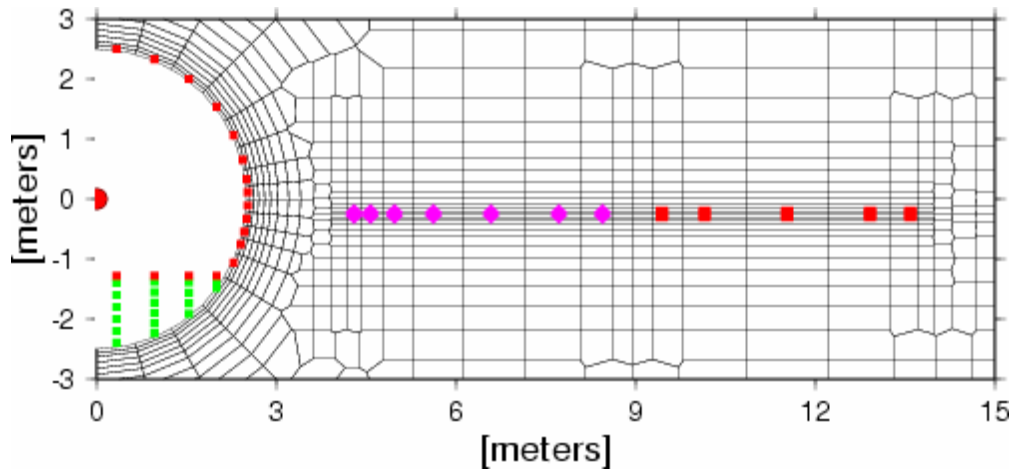


**Figure B1b.** Enlarged view of the numerical mesh showing the locations of grid blocks representing the heated drift, wing heaters, and concrete invert. Note: Inner (violet diamonds closer to drift) and outer wing heater (red squares) indicate grid block coordinates. Heat was applied to the drift center. Green squares indicate grid block locations for the concrete invert.

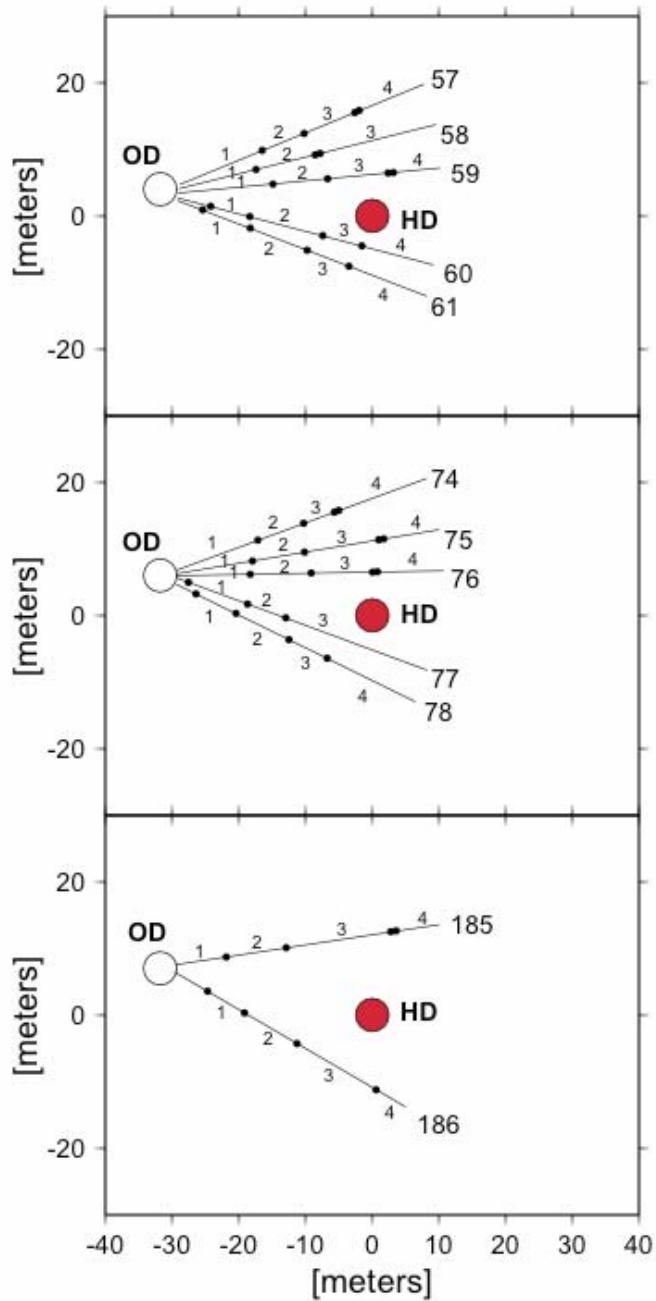
## B4.2 Heater power

In the Heated Drift, heat was applied solely to the drift-center grid block, which is connected to all surrounding grid blocks. The wing heaters are split into inner and outer zones, with more power applied to the outer zone to approximate the presence of an adjacent parallel drift. The positions of grid blocks representing heaters are shown in Figure B1b. The heating schedule was based on step-wise averages of the 10-day incremented power data. A 9-month initial period is set to the ambient temperature, corresponding approximately to the time that was required to set up the test. Intentional power reductions were directly accounted from the power data. Estimates were made of the duration of the longer (approximately greater than 1/2 day) temporary power outages. Table B1 gives the step-wise averaged power data implemented in the model simulations. Each time in Table 1 represents the initiation of a specific period of heating or power loss that continues until the succeeding time. The simulations were run for the full period of heating plus a 4-year period of cooling (shown by the hypothetical end time at the base of Table B1).

## B4.3 Hydrological and Thermal Parameters

Values of hydrological and thermal input data are listed in Table B2. The fracture tortuosity (0.7) is based on models of *in situ* testing data. This fracture tortuosity was modified for fracture-fracture connections by multiplication of the tortuosity by the fracture porosity of the bulk rock. This operation yields a better approximation for the fracture-to-fracture interconnection area (only for calculation of diffusive fluxes; the entire grid block connection area is used for calculating advective fluxes, because the bulk fracture permeability is used for flow calculations).

The capillary pressure in both fractures and matrix must reach some maximum, finite value upon complete dryout (zero liquid saturation). For fractures and matrix in the Tptpmn and Tptpll lithostratigraphic units (model units tsw34 and tsw35, respectively),



*NOTE: Borehole intervals are designated as 1, 2, 3, and 4 moving away from the Observation Drift (open circle designated “OD”). Temperature sensors (not labeled) are shown as the small closed circles, and are designated similarly to the intervals (i.e., sensor 60-4 is the 4<sup>th</sup> sensor from the Observation Drift). OD = Observation Drift; HD = Heated Drift.*

*Figure B2. Locations of hydrology boreholes, sampling intervals (numbered) and temperature sensors*

the limit is set by the calculated slope of the  $P_{cap}$  versus liquid saturation curve at a liquid saturation value equal to  $S_r + \epsilon$ . For these units,  $\epsilon$  values for the matrix yield maximum  $P_{cap}$  values of  $10^8$  Pa (Table B2); for fractures,  $\epsilon$  is set to 0.01 (maximum  $P_{cap}$  values around  $10^3$ – $10^4$  Pa).

The thermal conductivities of fracture and matrix grid blocks are calculated assuming a linear interpolation between dry and wet conductivities as a function of liquid saturation. These are the thermal conductivities for the solid + fluid system. For fractures, thermal conductivities are multiplied by the fracture porosity to account for the correct fracture-to-fracture connection area in calculations of heat conduction (i.e., this is needed because full grid block areas are input into the model). Fracture thermal conductivities are also reduced by a factor of 10 to account for the limited spatial continuity and connectivity between fracture grid blocks. The volume of the fracture continuum is, however, only a small fraction of the matrix continuum. Therefore heat conduction occurs primarily through the matrix continuum and, as a result, the model is not sensitive to the amount of heat conduction in fractures.

*Table B1. Step-wise averaged power data*

Date	Time (s)	Time (days)	Canister Power (watts)	WH (inner) Power (watts)	WH (outer) Power (watts)	Comments
3/5/97	0.00000E+00	0.00	0.0000	0.0000	0.0000	pre-test
						heaters turned on
12/3/97	2.35872E+07	273.00	1091.3740	1232.4007	1626.7690	
3/15/98	3.24000E+07	375.00	1091.3740	0.0000	0.0000	outage - right rib
3/16/98	3.25080E+07	376.25	1091.3740	1232.4007	1626.7690	
4/12/98	3.48192E+07	403.00	1077.9972	1198.5773	1582.1220	
8/10/98	4.51872E+07	523.00	1119.6842	1201.8035	1586.3807	
						power outage
1/27/99	5.98752E+07	693.00	0.0000	0.0000	0.0000	
1/27/99	5.99400E+07	693.75	1123.5789	1204.4465	1589.8693	
2/16/99	6.16032E+07	713.00	1102.5965	1189.0805	1569.5862	
						power outage
5/27/99	7.02432E+07	813.00	0.0000	0.0000	0.0000	
5/27/99	7.03080E+07	813.75	1102.5965	1189.0805	1569.5862	
						power outage
5/29/99	7.04160E+07	815.00	0.0000	0.0000	0.0000	
5/30/99	7.04808E+07	815.75	1087.8653	1155.5245	1525.2923	
						power outage
6/18/99	7.21440E+07	835.00	0.0000	0.0000	0.0000	
6/19/99	7.22088E+07	835.75	1087.8653	1155.5245	1525.2923	
						power outage
7/9/99	7.39584E+07	856.00	0.0000	0.0000	0.0000	
7/15/99	7.44768E+07	862.00	1087.8653	1155.5245	1525.2923	
						power outage
8/27/99	7.81920E+07	905.00	0.0000	0.0000	0.0000	
8/29/99	7.83216E+07	906.50	1087.8653	1155.5245	1525.2923	
						outage - right rib
11/22/99	8.57088E+07	992.00	1087.8653	0.0000	0.0000	
11/24/99	8.58816E+07	994.00	1087.8653	1155.5245	1525.2923	

(Continued at next page)

(Continued form the previous page)

2/11/00	9.27072E+07	1073.00	0.0000	0.0000	0.0000	power outage
2/11/00	9.27720E+07	1073.75	1078.8421	1184.6642	1563.7568	
3/2/00	9.44352E+07	1093.00	1029.1930	1115.3660	1472.2831	power reduction
3/12/00	9.52992E+07	1103.00	0.0000	0.0000	0.0000	power loss
3/13/00	9.54072E+07	1104.25	1029.1930	1115.3660	1472.2831	
5/2/00	9.97056E+07	1154.00	964.5263	1040.2813	1373.1713	power reduction
8/15/00	1.08778E+08	1259.00	917.3463	978.7397	1291.9364	power reduction
1/20/01	1.22429E+08	1417.00	0.0000	0.0000	0.0000	power outage
1/21/01	1.22515E+08	1418.00	917.3463	978.7397	1291.9364	
5/1/01	1.31155E+08	1518.00	875.5711	925.4672	1221.6168	power reduction
7/1/01	1.36426E+08	1579.00	0.0000	0.0000	0.0000	power outage
7/1/01	1.36490E+08	1579.75	875.5711	925.4672	1221.6168	
8/22/01	1.40918E+08	1631.00	826.8171	875.8317	1156.0979	power reduction
1/14/02	1.53446E+08	1776.00	0.0000	0.0000	0.0000	heaters turned off
1/14/06	2.79677E+08	3237.00	0.0000	0.0000	0.0000	cooling period end

NOTE: Each time represents the initiation of a particular period of heating (or power loss) that continues until the next time in the table. Data are for a 2-D vertical slice.

Table B2a. Summary of hydrological and thermal properties of repository units

Model	Layer	>	tsw33	tsw34	tsw35
Lithostratigraphic Unit >			Ttpul	Ttpmn	Ttpll
van Genuchten m (or )	$m_f$		0.633	0.633	0.633
residual saturation	$S_{lrf}$		0.01	0.01	0.01
satiated saturation	$S_{lsf}$		1.00	1.00	1.00
active fracture parameter	gamma		0.60	0.57	0.57
frequency	f (1/m)		0.81	4.32	3.16
fracture to matrix area	A ( $m^2/m^3$ )		4.44	13.54	9.68
tortuosity	t		0.7	0.7	0.7
epsilon (for max $P_{cap}$ )	$\epsilon$		0.01	0.01	0.01

Table B2b. Hydrological and thermal properties

Model	Layer	>	tsw33	tsw34	tsw35
Lithostratigraphic Unit	>		Ttpul	Ttpmn	Ttpll
MATRIX DATA					
permeability	$k_m$ ( $m^2$ )		6.57E-18	1.77E-19	4.48E-18
porosity	$\phi_m$		0.1425	0.1287	0.1486
van Genuchten	$a_m$ (1/Pa)		6.17E-6	8.45E-6	1.08E-5
van Genuchten m (or )	$m_m$		0.283	0.317	0.216
residual saturation	$S_{lrm}$		0.12	0.19	0.12
satiated saturation	$S_{lsm}$		1.00	1.00	1.00
epsilon (for max $P_{cap}$ )	$\epsilon$		0.138	0.091	0.216
rock grain density	$r_g$ ( $kg/m^3$ )		2358	2466	2325
rock grain specific heat	$C_p$ (J/kg-K)		985	985	985
dry conductivity	$\lambda_{dry}$ (W/m-K)		1.164*	1.419*	1.278*
wet conductivity	$\lambda_{wet}$ (W/m-K)		1.675*	2.074*	1.890*
tortuosity	$t$		0.2	0.2	0.2
FRACTURE DATA <sup>1</sup>					
permeability	$k_f$ ( $m^2$ )		7.80E-13	3.30E-13	9.10E-13
porosity	$\phi_f$		5.8E-3	8.5E-3	9.6E-3
van Genuchten	$a_f$ (1/Pa)		1.59E-3	1.04E-4	1.02E-4

Note: <sup>1</sup> Fracture thermal properties are derived using matrix properties. \* Bulk conductivities converted from grain conductivity values and lithophysal porosities, using  $K_{bulk} = K_{grain} (1 - \phi_{lith}) + \phi_{lith} K_{air}$ , with  $K_{air} = 0.028$  (W/m-K) (extrapolated at 50°C from Lide 1993).

## B4.4 Geochemical input data

Thermodynamic data and kinetic data are given in BSC (2003). Except for smectites, the chemical and physical properties of minerals that form solid solutions are approximated by their individual endmember compositions and properties. Because smectite endmembers are (individually) near equilibrium with pore waters, some of the smectite endmembers could be calculated to precipitate while others dissolve. For this reason, an ideal solid-solution model is implemented for smectite (Na, Ca, and Mg endmembers), with each endmember's activity equaling its mole fraction. Treating the smectite as a solid solution, results in individual smectite endmembers either all dissolving or all precipitating, providing a better physical representation of dissolution/precipitation processes. Feldspar solid solutions are not considered because albite (Na-feldspar) and anorthite (Ca-feldspar) are generally strongly undersaturated in the simulations, and thus their dissolution rates are governed primarily by the kinetic rate constant rather than the saturation index (Equation B5).

## **B4.5 Initial and boundary conditions: hydrological and thermal**

Steady-state liquid saturations, temperatures, and thermal-hydrological properties are listed in Table B2. The top and bottom boundaries were set to constant temperature, pressure, and liquid saturation, based on steady-state values obtained from simulations of a 1-D column extending from the land surface to the water table. The top boundary of the 2-D model extends 150 m above and below the drift center, but does not reach either the land surface or the water table. Under these conditions, the percolation flux at the top boundary is approximately 0.5 mm/yr. The bottom boundary condition is open to gas and to liquid flow. The side boundaries of the domain are located 81.5 m away from the drift center on each side (outside of the test influence area) and are no-flux for mass and heat. The air pressure and temperature in the observation drift are set to constant values, and therefore do not reflect temporal fluctuations in barometric pressure or tunnel air temperatures. The Heated Drift wall is open to advection and conduction of heat and mass (e.g., air, water vapor, and CO<sub>2</sub>).

## **B4.6 Initial and Boundary Conditions: Geochemical**

Aqueous and gaseous species concentrations in the rock were initially set to a uniform value, based on the measured pore water composition and calculated equilibrium values for CO<sub>2</sub> and some aqueous species. The Heater Alcove and Observation Drift CO<sub>2</sub> concentrations were fixed to approximately that of the atmosphere. The Heated Drift CO<sub>2</sub> concentration was initially set to the same value as that in the Observation Drift, but was allowed to exchange CO<sub>2</sub> with the Heater Test Alcove and with the surrounding rock.

Both the top and bottom boundary conditions are open to gas and aqueous species transport. The top and bottom boundaries were also set so that no mineral reactions take place (and therefore no changes in aqueous species concentrations occur as a result of mineral-water reactions). Their volumes were set to extremely large values, so that they act essentially as constant concentration boundaries. The side boundaries are no-flux for gas and aqueous-species transport.

# **B5. THC Simulation results and comparisons to data**

## **B5.1 Thermal and hydrological evolution**

The main driving force for changes in the hydrological and chemical behavior of the system is the strong thermal load applied to the system. The resulting changes in temperature, liquid saturation, and gas-phase composition lead to changes in the chemistry of water and gas, as well as mineral dissolution and precipitation. Key aspects of the thermal-hydrological behavior of the DST that drive the chemical evolution of the system are discussed briefly in this section.

The modeled temperatures in the drift reflect the heat input at the drift center (at the approximate location of the electrical canister heater) and subsequent heat transfer to the drift wall (Figure B3). Differences in temperature between the drift center and the drift wall (Figure B3) near the top (drift crown) are approximately 20°C, similar to the differences observed between electrical canister temperatures and drift-crown

temperature measurements. Sharp temperature drops are the result of power losses, heater failures, and/or intentional power reductions.

Drift-wall temperatures predicted by the two-dimensional model eventually exceed the maximum measured values by about 20°C. However, predicted temperatures in the rock are typically closer to measured values (Figure B4). There are several reasons for the elevated temperature in the drift. First, the 2-D cross section can only approximate the exchange of heat through the rock along the axis of the DST. Second, heat lost through the bulkhead by a combination of advection and diffusion is uncertain and can only be approximated using porous flow equations in a basically one-dimensional manner and with a 2-D model. Therefore, this model is most applicable to areas near the center of the test—away from both the bulkhead and the opposite end of the Heated Drift.

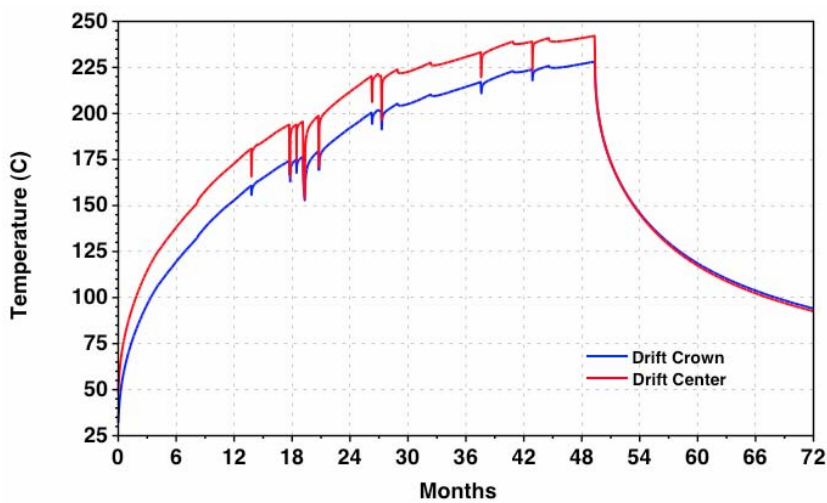


Figure B3. Drift Center and Drift Crown Modeled Temperatures over the First Six Years of the DST

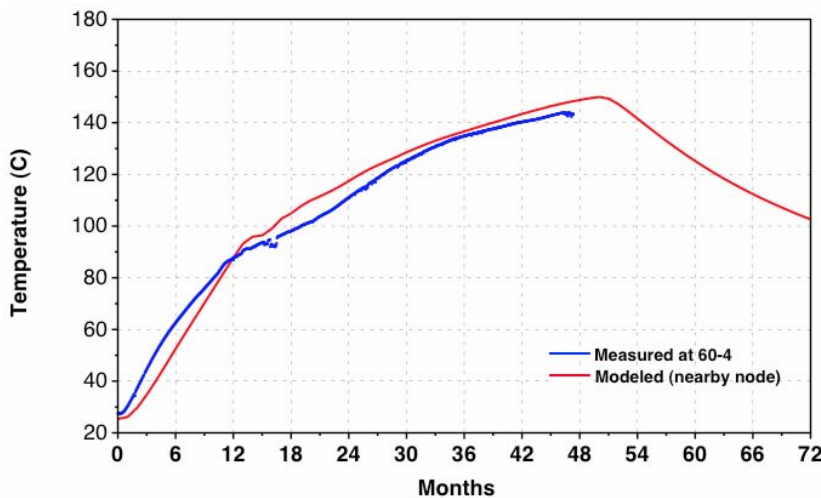


Figure B4. Comparison of Modeled and Measured Temperatures over Time for the Sensor Located at Hydrology Borehole Packer 60-4. NOTE: Modeled Temperatures are for a Nearby Grid Block. Temperature sensor location is shown in Figure B2.

Other factors that control the temperature response of the drift wall include thermal properties (conductivity, heat capacity) of the rock and the representation of heat transfer processes in the drift (approximate treatment of thermal radiation and convection). The rate of temperature increase at the drift wall could only be approximated because the model employs a temperature-independent rock heat capacity, does not consider thermal radiation, and does not include a rigorous model for gas convection in the drift. However, the comparison of temperatures measured in the rock, compared to the modeled temperatures, provides the true test of the validity of the model for heat transfer to the rock (Figure B4).

The modeled distributions of fracture and matrix liquid saturation (with temperature contours overlain) are shown in Figures B5a–d. The plots correspond to one and four years from the initiation of the heating phase. The extent of the dryout zone increases over the heating period and is larger in the fractures than the matrix. A wider spatial interval between the 90°C and 100°C isotherms indicates the presence of an isothermal boiling/condensation (heat pipe) zone, which is especially well developed above the wing heaters. An extensive drainage zone extending several tens of meters in the fractures below the heaters contrasts with a very narrow high-saturation zone above the heaters, where water is continuously diverted around the heated zone. The narrow band of increased fracture saturation above the heaters is characterized by temperatures of about 90–95°C. Typically, water was collected from hydrology boreholes when this heat-pipe zone intersected the borehole intervals.

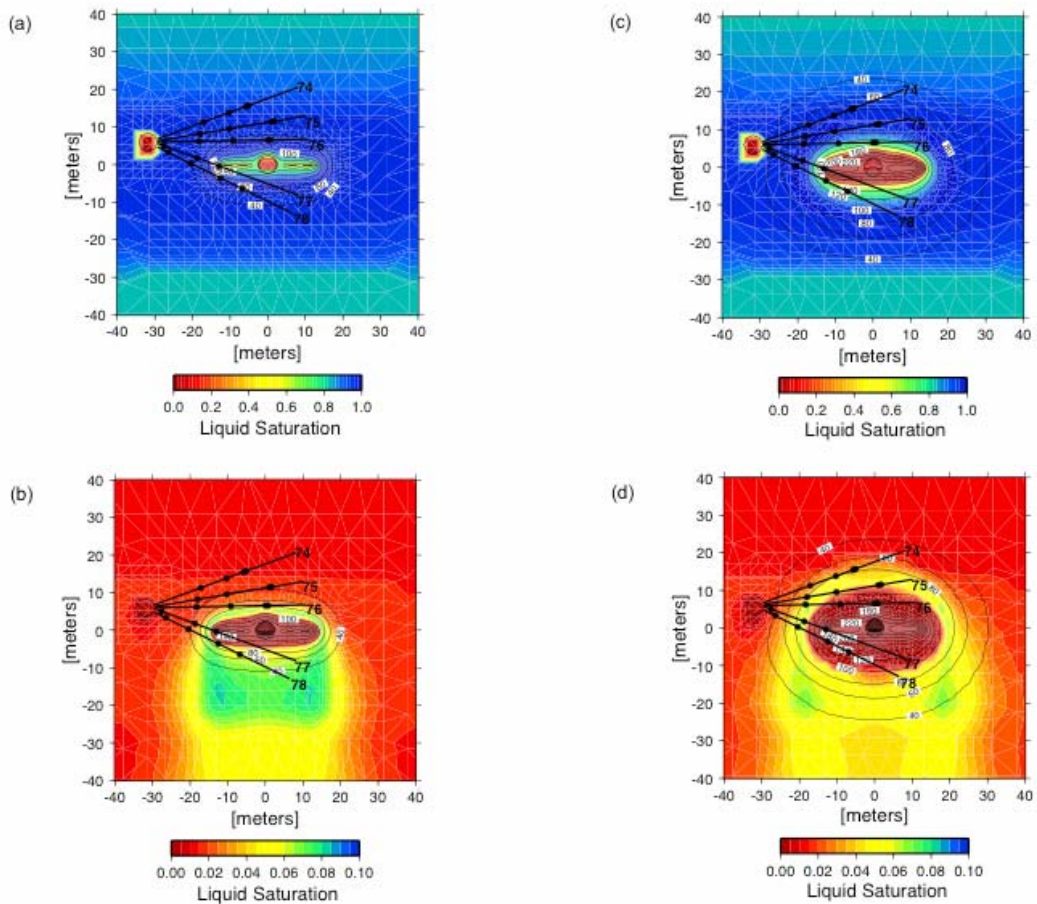


Figure B5. Liquid saturation (colors) and temperature (contour lines) in the dst (base case) at one year (matrix – a, fracture – b) and at four years (matrix – c, fracture – d)

## **B5.2 Gas-phase CO<sub>2</sub> evolution: measured compositions and simulation results**

The evolution of CO<sub>2</sub> concentrations in the gas phase is discussed in this section. Simulation results are compared to concentrations measured in gas samples taken from boreholes during the entire heating phase of the DST. The concentration of CO<sub>2</sub> in the gas phase is a function of temperature, pressure, aqueous-phase chemistry, mineral-water reactions, and advective and diffusive transport. Numerous measurements of CO<sub>2</sub> concentrations in gas collected from the DST have been made as a function of space and time, and therefore, a more complete comparison of the model results to CO<sub>2</sub> data can be made than to the relatively fewer number of water-chemistry measurements. CO<sub>2</sub> concentrations in gases collected from the DST also provide a qualitative measure of the influence of atmospheric gas on the system, because of the relatively low and constant value in the atmosphere ( $\cong$  400 ppmv).

### **B5.2.1 Gas sampling and CO<sub>2</sub> measurements**

Gas sampling, analytical methods, and compositional data are discussed in Section 6.3.4.2 of BSC (2002a). Gas samples were taken from several meter-long borehole intervals that spanned a wide range of temperatures as a result of their orientation relative to the heaters. As part of the sampling procedure, the gas samples had much of their water vapor removed before analyses were performed, and therefore measured CO<sub>2</sub> concentrations are for the noncondensable gas fraction. The noncondensable gas fraction is very high (>95%) at the ambient temperature of about 25°C, but may drop to extremely low values (< 1%) under boiling conditions. Hence, reported CO<sub>2</sub> concentrations at temperatures close to boiling are much higher than if the measurements were made on a “complete” gas composition (air + CO<sub>2</sub> + H<sub>2</sub>O). This effect must be considered when comparing model results to measured values.

### **B5.2.2 Modeled spatial distribution of CO<sub>2</sub>**

Modeled distributions of CO<sub>2</sub> concentrations (log ppmv) in fractures are shown at yearly intervals during the heating phase (Figure B6) and during the cooling phase (Figure B7). Over the heating phase of 4 years, a region of highly elevated CO<sub>2</sub> concentrations, centered approximately at the 60°C isotherm, is seen to move gradually outward from the heaters. Outside this region, CO<sub>2</sub> concentrations gradually decrease to the ambient value in equilibrium with pore water (approximately 1,000 ppmv). Maximum CO<sub>2</sub> concentrations of around 50,000 ppmv are located above and below the wing heaters and the Heated Drift. Towards the heaters, CO<sub>2</sub> concentrations drop off more sharply with increasing temperature, decreasing to values below 10 ppmv. This sharp decline takes place as a result of the CO<sub>2</sub> degassed during heating of the pore water, its transport outward, and the displacement of air and CO<sub>2</sub> by steam generated during boiling. The zone of maximum CO<sub>2</sub> concentrations also transects the hydrology borehole intervals as it migrates outwards, with some intervals exhibiting a two order-of-magnitude variation between them.

The effect of the atmospheric CO<sub>2</sub> concentration of the gas in the Observation Drift on its surroundings is evident up to about 10 m from the drift wall. However, effects on the fracture gas composition are relatively minor beyond about 5 m from the drift wall.

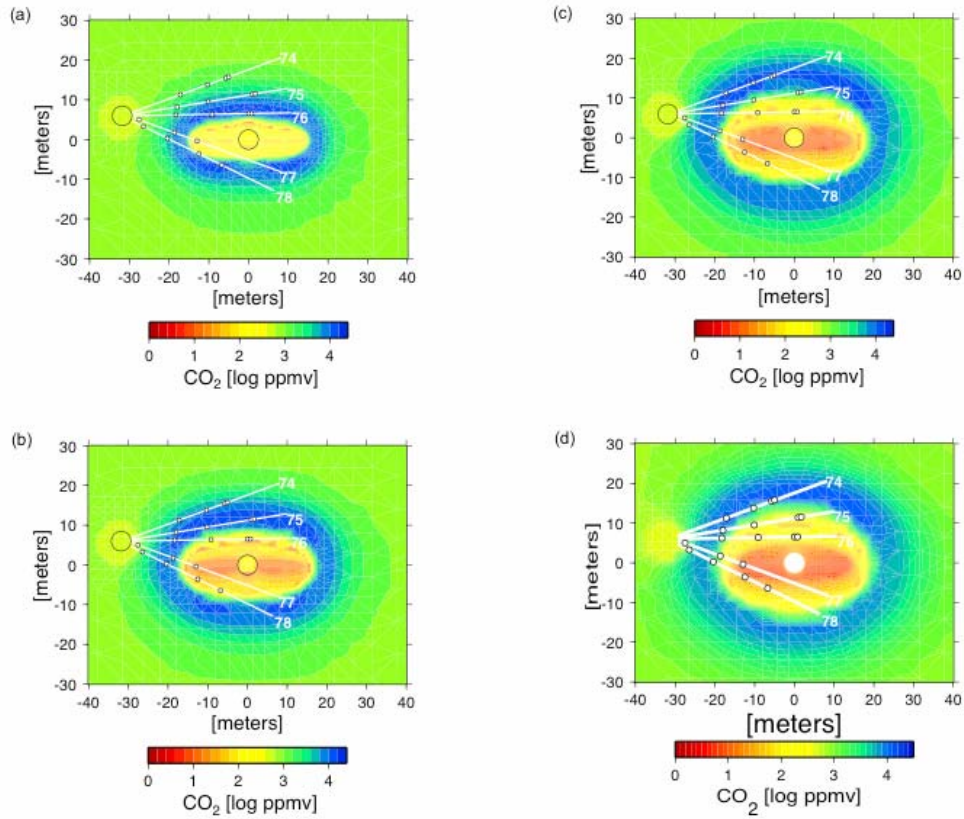


Figure B6. Modeled Gas Phase  $\text{CO}_2$  Concentrations (Log ppmv) in Fractures during the Heating Phase of the DST at 1, 2, 3, and 4 years

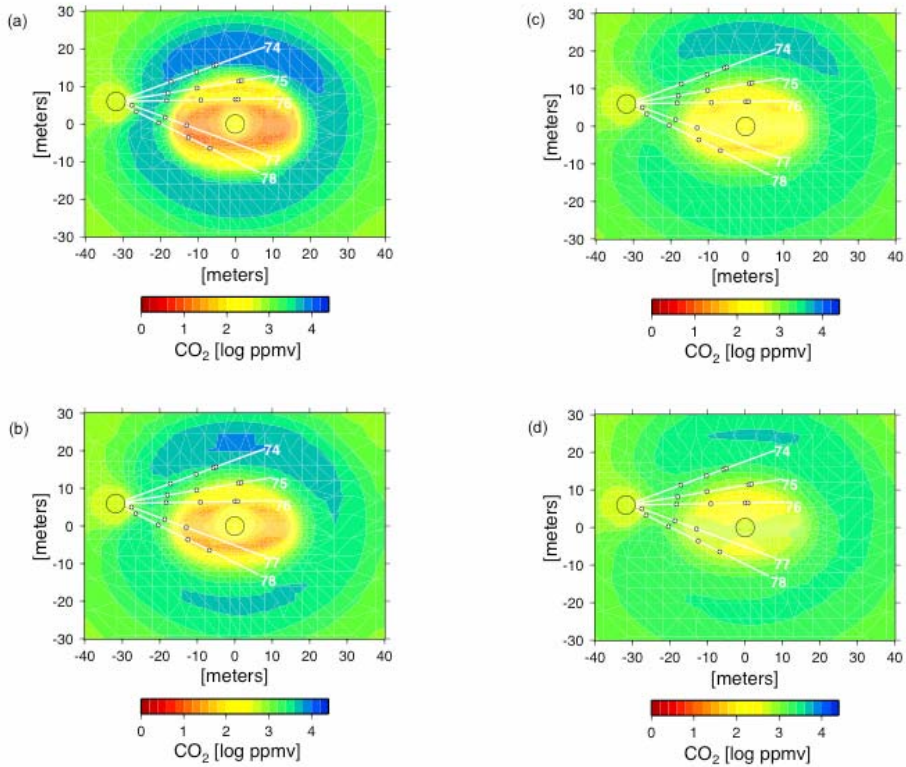


Figure B7. Modeled Gas Phase  $\text{CO}_2$  Concentrations (Log ppmv) in Fractures during the Cooling Phase of the DST at 5, 6, 7, and 8 years

Carbon dioxide concentrations in the Heated Drift stay close to the atmospheric value, owing to transport (advection and diffusion) between the Heater Test Alcove (set to atmospheric CO<sub>2</sub>) and the Heated Drift.

The modeled cooling phase of the DST (Figure B7) is characterized by a gradual re-equilibration of CO<sub>2</sub> concentrations in the rock, via cooling, gas-phase diffusion, and flow of gas and water. Exchange of atmospheric gas among the Heated Drift, the Heater Test Alcove, and the rock around the Heated Drift is clearly evident.

### **B5.2.3 Modeled and measured CO<sub>2</sub> concentrations over time**

Validation of the DST THC Model for the prediction of the temporal evolution of CO<sub>2</sub> concentrations was performed by comparison of measured values from intervals repeatedly sampled from February 1998 through January 2002 to model results. Because the measured concentrations come from borehole intervals that are several meters long, and not from a specific location, model data are chosen from the grid block closest to the center of the interval. If a grid block is not centered on the borehole, a grid block closest to the center is chosen on the outer (cooler) side of the borehole. Grid blocks on the cooler side should compare more closely to the measured data because the 2-D model, having no heat loss in the rock perpendicular to the drift, produces temperatures that are somewhat higher than the measured temperatures after approximately the first year of heating. However, measured temperatures may be higher prior to that time (refer back to the temperature comparison in Figure B4).

To assess the effect of water extraction from the gas during collection, measured CO<sub>2</sub> concentrations were corrected for the approximate amount of water removed during chilling of the gas sample from the temperature of the sampling interval to 25°C. The method assumes that the gas is vapor-saturated, removes the appropriate amount of water vapor to the amount at saturation at 25°C, and adds some of the CO<sub>2</sub> into solution (the condensate) as HCO<sub>3</sub><sup>-</sup>, based on the equilibrium partitioning of CO<sub>2</sub> into H<sub>2</sub>O. The actual temperature of the chiller was 4°C; however, the efficiency of the unit was such that not all water was taken out when the gas was at boiling temperatures (BSC 2002a). Therefore, for consistency, the chill temperature was set to 25°C for all samples. Because the difference in water-vapor content between 25°C and 4°C is small, this approximation is valid. For samples with temperatures below approximately 60°C, the correction is very small; however, at temperatures near boiling, the correction may be close to an order of magnitude.

The effect of the correction on the measured CO<sub>2</sub> concentrations is a gradual (but increasing) reduction up to the boiling temperature, where the sharp “second” spike in the uncorrected data largely disappears. It is clear that the correction to the measured concentrations substantially improves the comparison to the modeled data at higher temperatures. Figure B8 shows an example of the effect of the correction on the CO<sub>2</sub> concentrations for borehole interval 75-3.

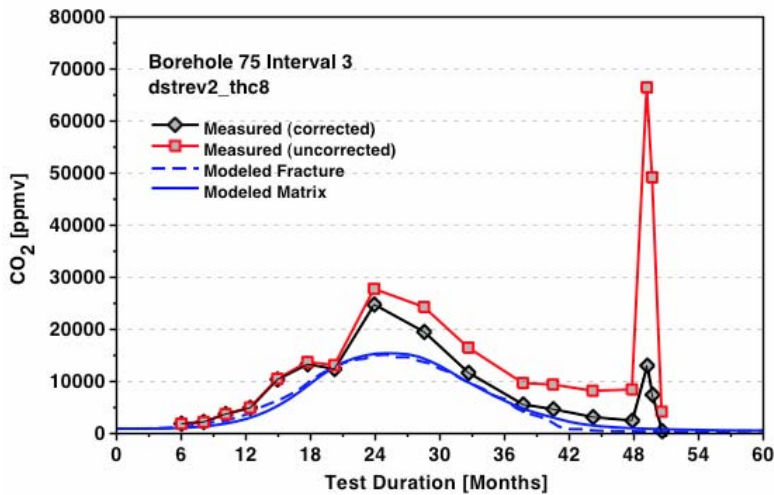


Figure B8. Comparison of Measured and Corrected Concentrations for Borehole Interval 75-3 and the Model Simulation Results

Figure B9 shows measured CO<sub>2</sub> concentrations that have been corrected for the effect of water-vapor condensation during sample collection. Modeled CO<sub>2</sub> concentrations shown for 74-3 are given as an average of the values from cooler and hotter grid blocks, because no grid blocks have centers close to the interval midpoint. The measured concentrations show a sharp increase at 24 months (Figure B9a). This is partly a result of the relatively low value around 21 months, which apparently was affected by an earlier temporary power loss (see Table 2 for dates of power losses). After 24 months, the measured concentrations declined moderately, whereas the modeled concentrations continued to rise, albeit more slowly. This decrease in measured CO<sub>2</sub> concentrations may reflect the power reductions that were implemented during 2000. The trend in modeled CO<sub>2</sub> concentrations for 75-3 is similar to the measured trend, with a sharp reduction in concentration after 24 months (Figure B9b). The upper interval closest to the heaters is 76-3, in which the measured data (Figure B9c) shows a large decline after 21 months, which has predicted to occur earlier than actually observed. This difference may between prediction and observation result from the grid block being closer to the interval in 76-3 than in 74-3 and 75-3, and therefore slightly hotter at a given time. In the hottest interval (76-3) the concentrations remained low from 2 years after heating was initiated until after the cooling phase had begun. Except for one sample that may have been predominantly water vapor, similar but delayed behavior took place in 75-3.

## B5.3 Aqueous species evolution

### B5.3.1 Chemistry of waters sampled during the Drift Scale Test

Water samples were collected from several hydrology boreholes during the heating phase of the DST. Collection dates, volumes, and field measurements (e.g., pH) for all water samples are presented in Table 6.3.4.1-1 of BSC (2002a). Cation and anion analyses of the water samples are given in Table 6.3.4.1-2) of the same report. The latter table lists all samples that were analyzed, regardless of their origin. In particular, many samples were collected from borehole intervals above boiling temperatures and were

clearly derived from water vapor that condensed in the tubing leading out of the interval. In most cases such samples are clearly recognizable from the water samples pumped directly out of boreholes (and in contact with rock), based on (1) their significantly lower pH (most below pH 5) relative to “true” water samples (nearly all above pH 6), (2) their extremely low anion and cation content (total dissolved solids around 10 ppm or less), and (3) very low total Si concentrations (most much less than 10 mg/L) compared to water samples having total Si concentrations mostly greater than 40 mg/L.

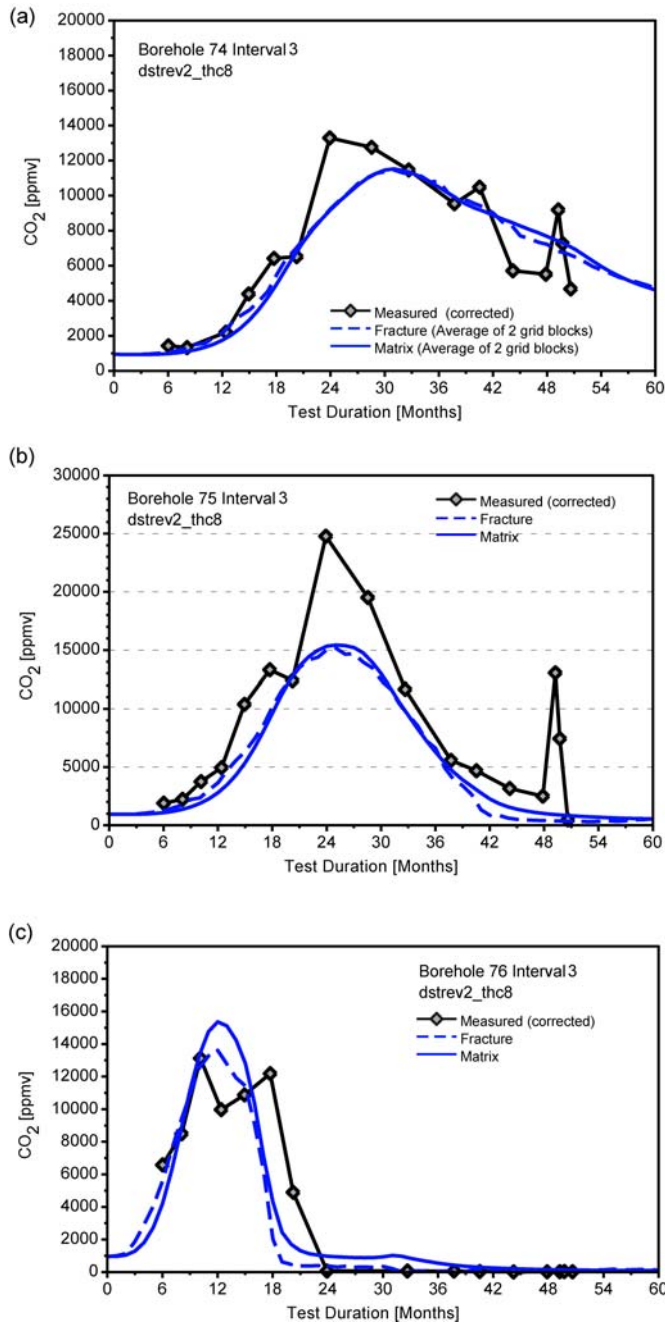


Figure B9. Comparison of Modeled CO<sub>2</sub> Concentrations in Fractures to Measured (Corrected) Concentrations in Boreholes: (a) Borehole Interval 74-3 (Average of Bounding Grid blocks); (b) Borehole Interval 75-3; (c) Borehole Interval 76-3

In this report, chemical analyses of water samples that have compositions indicating that they were wholly or mostly derived from water that had resided in a borehole (rather than formed during condensation of water vapor in the collection tube) are compared to model results in the following sections. The intervals where these waters were collected are shown as the blue shaded zones in Figure B10. The water samples collected during the test were obtained from zones that were hotter than the temperatures given for the samples, because the samples cooled substantially as they were pumped out of the rock through the sample collection tubing, and into the sample containers. These water samples are considered to be representative of fracture waters produced by THC processes in the region around the DST. However, the borehole intervals from which the waters were collected are approximately 8-10 m in length and at times have temperatures several tens of degrees different at each end. Therefore, vapor flow from the hot end to the cool end of an interval, accompanied by condensation and reaction with the rock lining the borehole, could account for some of the water found in the boreholes. Because the borehole surface mineralogy is not identical to the fracture surface mineralogy, the water chemistry in the borehole may have some differences to the chemistry of water in the fractures. Yet, because the rock surface in the borehole was freshly drilled, it may be more reactive with respect to silicate mineral reactions, hence potentially producing higher concentrations of species making up the silicate mineral phases.

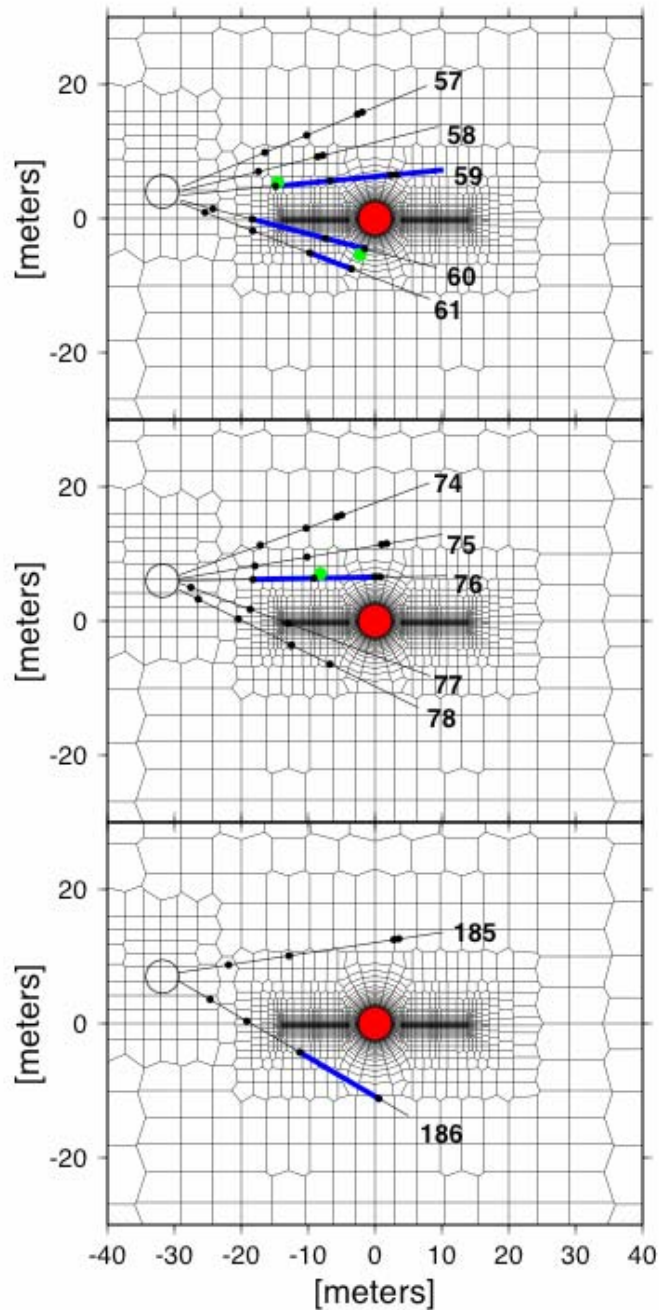
Further discussion of water chemistry in the DST and comparisons to model results is given in the following sections.

### **B5.3.2 Evolution in the pH of waters from the DST**

In this section, model simulations of the evolution of pH in space and time are shown, followed by comparisons of pH measurements of waters collected from boreholes and model results at specific locations. The modeled spatial distribution of pH in fracture water at various times during the heating phase is shown in Figure B11. The times correspond approximately to the dates when water was sampled from hydrology borehole intervals, which are also highlighted. Based on the compositions of ambient pore water ultracentrifuged from the rock in the DST block, the pH of waters in the region of the DST likely started out between approximately 7.8 and 8.3 (Table B3). The initial pH of the water used in the DST THC Model simulation is approximately 8.3. The most obvious effect of heating is a reduction in pH to about 7.2 in the condensate region, corresponding approximately to the increases in CO<sub>2</sub> concentrations shown in Figures B6 and B9. As for the CO<sub>2</sub> concentrations, the low pH zone increases in size and moves outward with time. Close to the dry-out zone, the pH of the water increases, owing to boiling, degassing, and outward transport of the CO<sub>2</sub>. Hydrolysis reactions, in which anhydrous minerals such as feldspars react to form clays or zeolites, also result in a rise in pH. Therefore, the reaction rates of aluminosilicate minerals are important for the pH evolution.

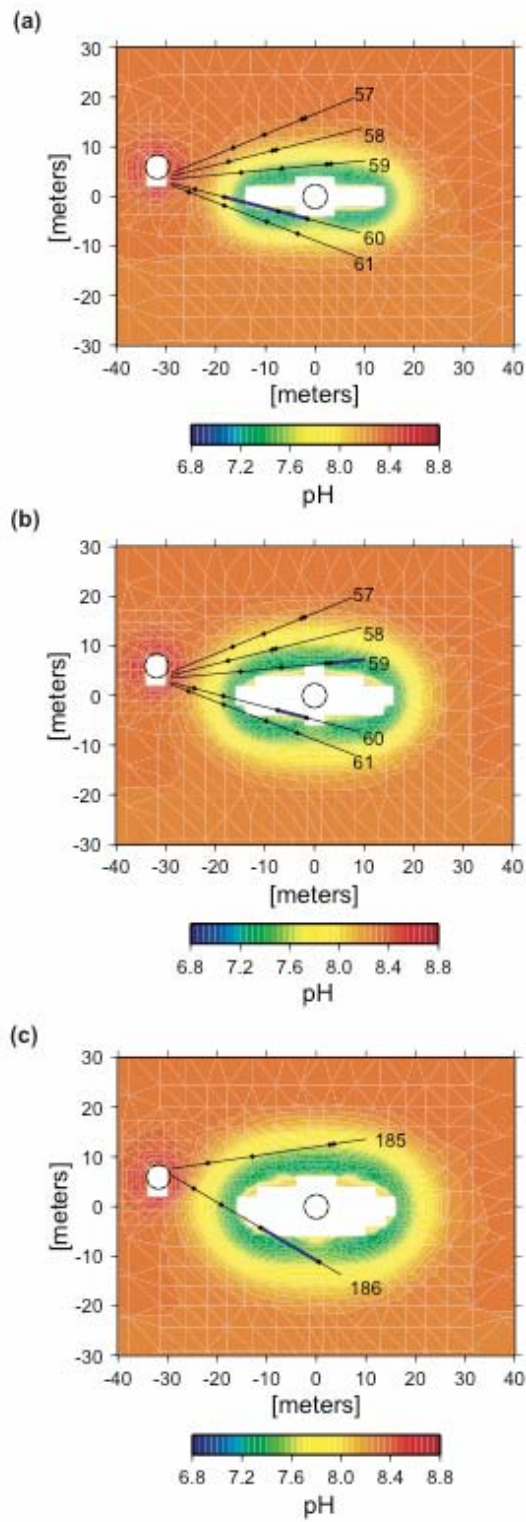
Modeled pH values are shown for borehole intervals 60-3, 59-2, and 76-3 in Figure B12. The modeled trends in pH are similar to the measured pH values, but the minimum pH is not as quite as low as that measured. Yet the differences between the measured and modeled pH values are generally less than one pH unit, within a fairly narrow range of approximately pH 6 and pH 8. The early trend to lower pH in 60-3 is related to the addition of condensate to this area and to increases in CO<sub>2</sub> in the gas phase (caused by boiling closer to the heaters and diffusive and advective gas transport outwards). Later increases in pH are related to boiling of the water in this area, leading to a reduction in

CO<sub>2</sub> concentrations as the temperature reaches boiling and the zone finally dries out. The model results for interval 60-3, showing complete dry-out at approximately 18 months, are consistent with the observation that water was absent from this interval shortly after the last sample was collected, after 16 months of heating.



NOTE: Locations where comparisons were made to measured compositions are shown as green circles. The Heated Drift is shown in red.

Figure B10. Zones where water was collected from hydrology boreholes (thick shading in blue) superimposed on the model mesh



NOTE: The intervals where water was sampled are more thickly shaded (in blue). Areas of zero liquid saturation are blanked out in white.

Figure B11. Modeled distribution of pH in fractures at various times when water was sampled from hydrology borehole intervals: (a) 6 months, (b) 11 months, and (c) 14 months

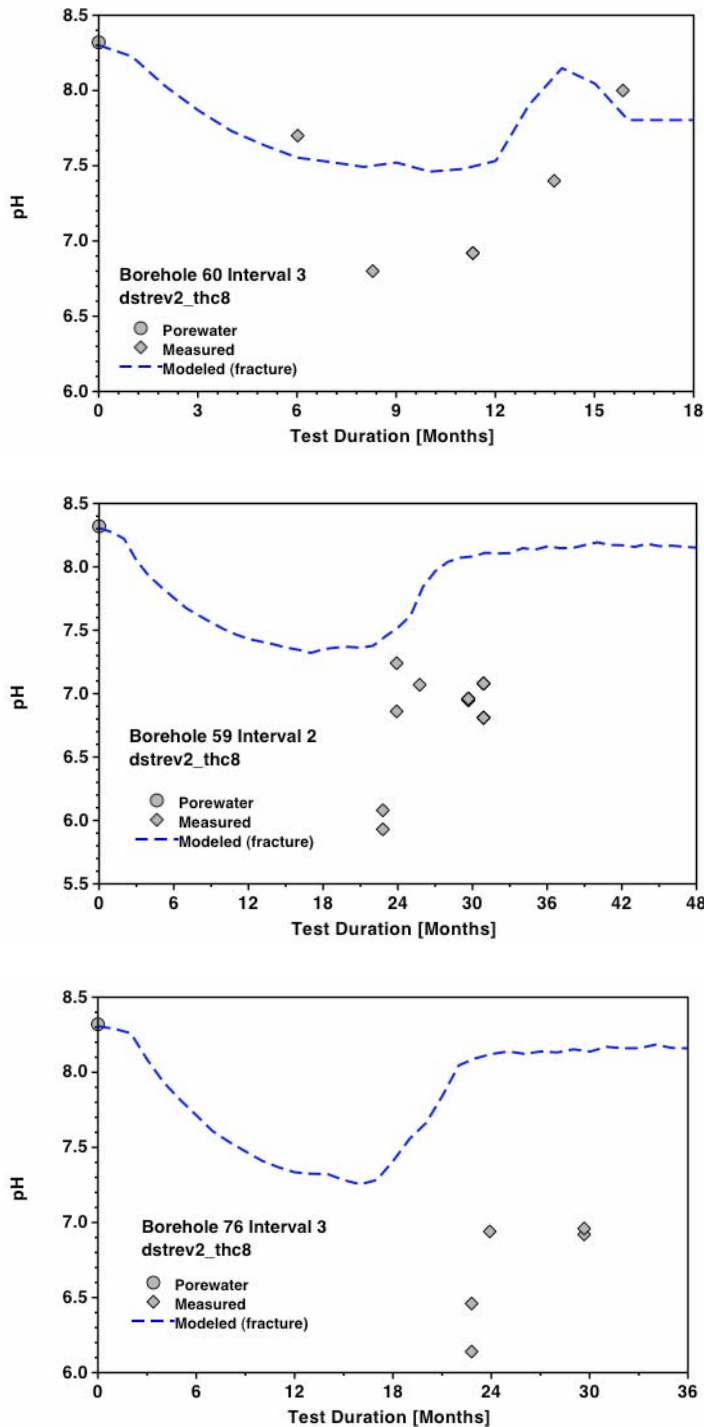
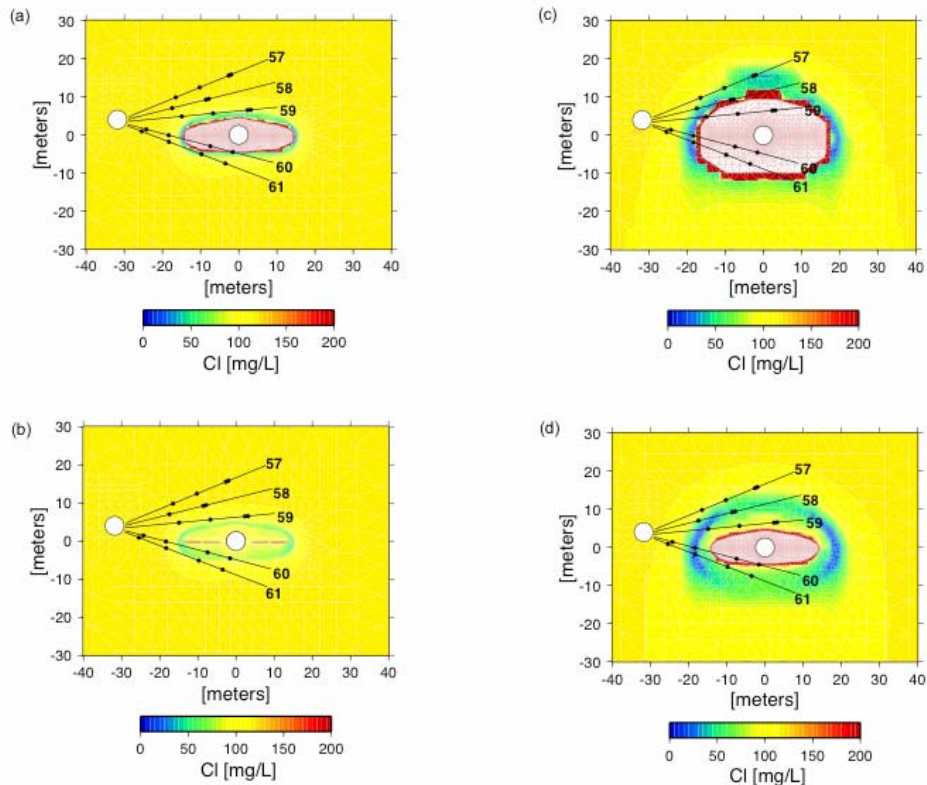


Figure B12. Comparison of Measured pH in Water Samples Collected from BoreholeIntervals (a) 60-3, (b) 59-2, and (c) 76-3 to Modeled Fracture Water pH. Note: The ambient pore-water pH is approximately 8.3.

In 59-2 and especially in 76-3, the drop in pH is considerably earlier than in the measured pH values. Part of this discrepancy is related to the higher modeled temperatures after one year (compared to those measured) resulting in an earlier arrival of the condensation “pulse” from the advancement of the boiling zone. Higher pH values may also result from the larger reaction rates for aluminosilicates at higher temperatures.

### B5.3.3 Evolution of anion and cation concentrations

The effects of dilution through condensation of pure water vapor, increases in concentration caused by boiling, and fracture-matrix interaction can be assessed by examining the variation in conservative species such as chloride ( $\text{Cl}^-$ ) and sulfate ( $\text{SO}_4^{2-}$ ). These species are conservative because chloride and sulfate-bearing minerals, such as halite and gypsum (or anhydrite), are not present in the rock initially and precipitate only under more saline conditions, expected only at the final drying stages. The modeled spatial variations in  $\text{Cl}^-$  concentrations in the fractures and matrix are plotted in Figure B13, at times of 1 year and 4 years during the heating phase. The main effect is a marked decrease in  $\text{Cl}^-$  concentrations within fractures in the condensation and drainage zones. In the matrix, there is significant dilution in the condensation zones, and significant increases in concentration near the edge of the dry-out zone.



NOTE: Areas of zero liquid saturation are blanked out in white.

Figure B13. Modeled distribution of  $\text{Cl}^-$  in fractures and matrix at one and four years during the heating phase of the DST: (a) fracture—1 year, (b) matrix—1 year, (c) fracture—4 years, and (d) matrix—4 years

Comparison of modeled and measured chloride and sulfate concentrations for borehole intervals 60-3, 59-2, and 76-3 are shown in Figures B14 and B15. The model results capture the overall trend of dilution, or fracture-matrix interaction in the system (compared to the initial matrix pore water), for both chloride and sulfate. The largest discrepancy in interval 60-3 is at the earliest time, when the first waters collected are more dilute than the modeled fracture waters. However, compared to the modeled

concentrations of  $\text{Cl}^-$  and  $\text{SO}_4^{2-}$  in matrix water, the fracture waters are more dilute and quite similar to the samples collected from the boreholes. This can be attributed to pressure buildups in the matrix and reduced vapor transport. The reduction in vapor transport out of the matrix led to lower liquid saturations in the fractures and a weaker dilution effect on the ambient fracture pore water. In borehole interval 59-2, the earliest collected samples are more closely matched than the later collected samples, although the overall trend is still captured reasonably well. The sharp increase in modeled concentrations at later times is a result of boiling and evaporative concentration.

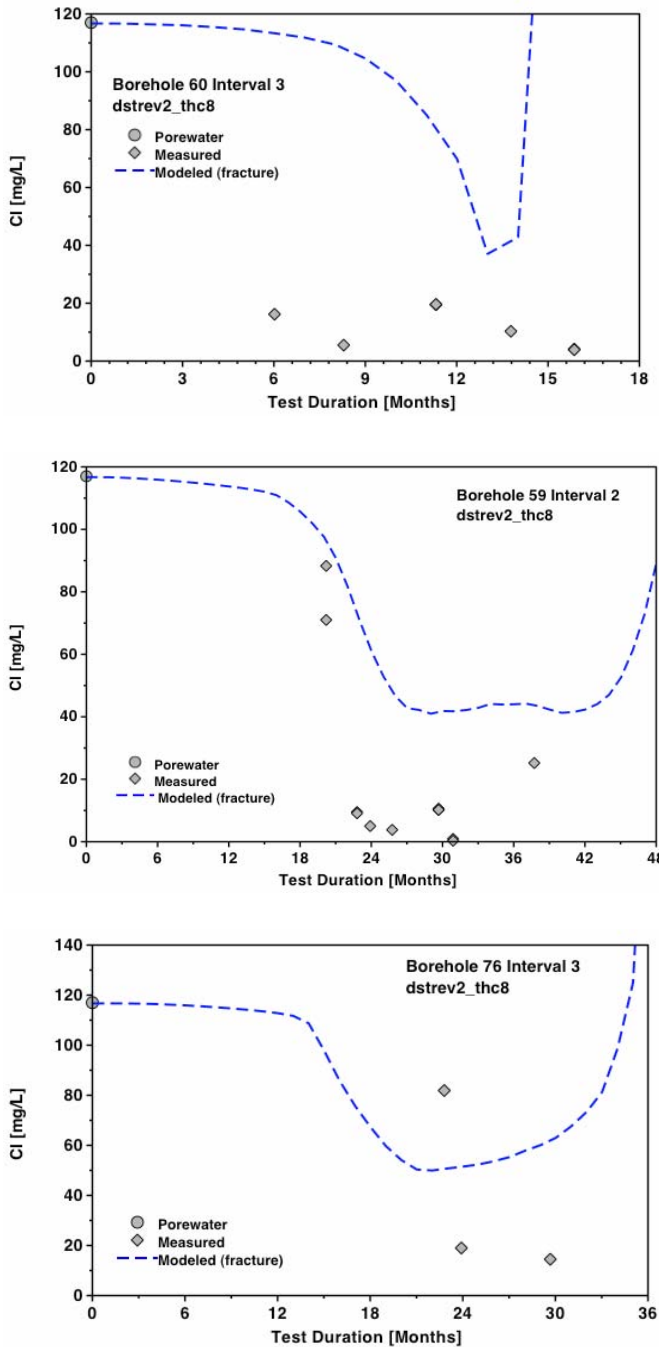


Figure B14.  $\text{Cl}^-$  concentrations (mg/l) in water samples collected from borehole intervals (a) 60-3, (b) 59-2, and (c) 76-3 compared to modeled fracture water  $\text{Cl}^-$

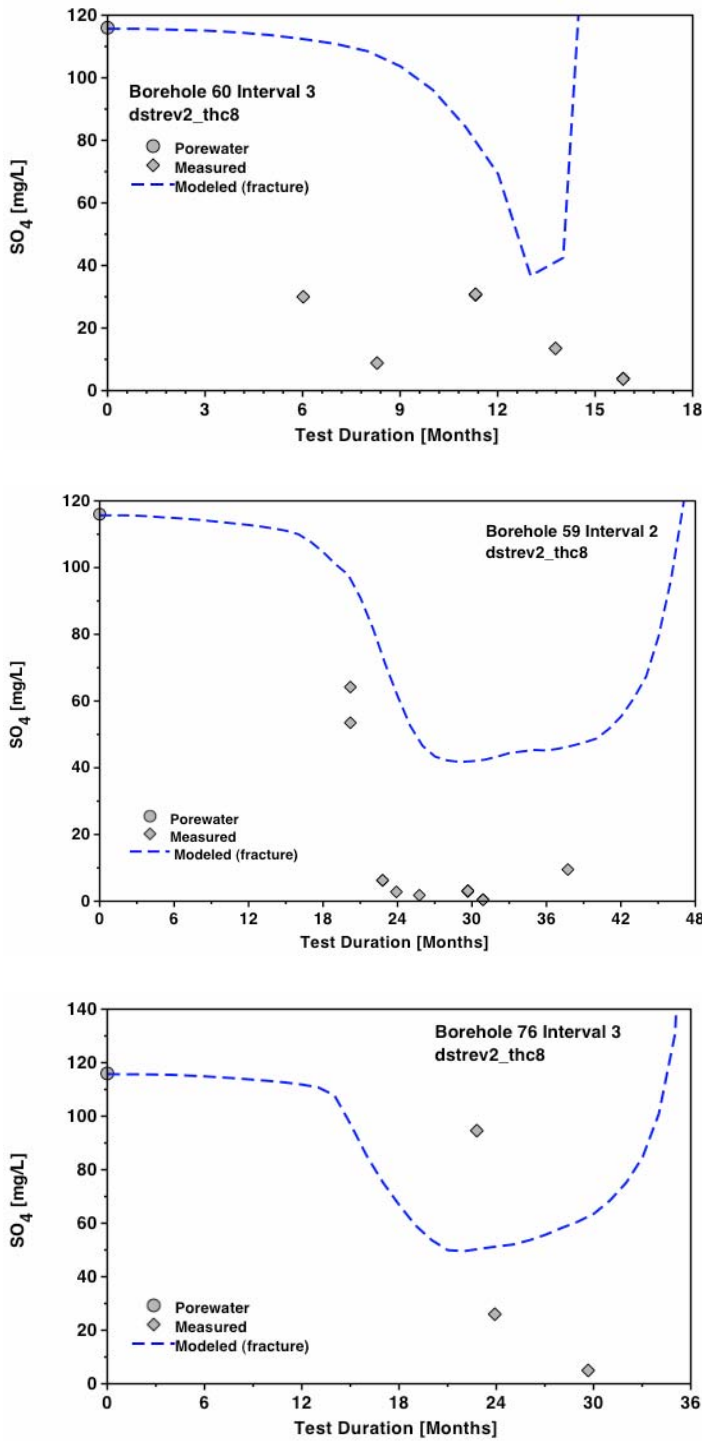


Figure B15.  $SO_4^{2-}$  concentrations (mg/L) in water samples collected from borehole intervals (a) 60-3, (b) 59-2, and (c) 76-3 compared to modeled fracture water  $SO_4^{2-}$

Measured sodium concentrations ( $Na^+$ ; Figure B16) are also much lower than in the initial pore water. However, the extent of dilution in interval 60-3 is by only a factor of about three to six times, whereas for  $Cl^-$  it was from about six to about 20. This difference indicates some contribution of water-rock interaction to the  $Na^+$  concentrations. The origin of the sodium in the DST waters could be alkali feldspar and/or reaction or exchange with clays. In the model simulations, the main source of  $Na^+$  is from alkali feldspar dissolution. As in the  $Cl^-$  and  $SO_4^{2-}$  variations over time, the

sharp rise to higher concentrations at later times is a result of rapid dry-out.  $\text{Na}^+$  concentrations (Figure B16) are elevated with respect to the modeled concentrations in the 60-3 and 59-2 boreholes, but are closer to the modeled values in borehole interval 76-3. The shape of the modeled  $\text{Na}^+$  curve shows an increase with temperature, prior to the main condensation pulse. This increase clearly results from the higher reactivity of albite, which also leads to increases in pH and a reduction in the partial pressure of  $\text{CO}_2$ . In the actual rock, it is likely that albite had undergone preferential weathering over several million years of infiltration and is coated by later-formed clays, silica polymorphs, and Ca-rich zeolites.

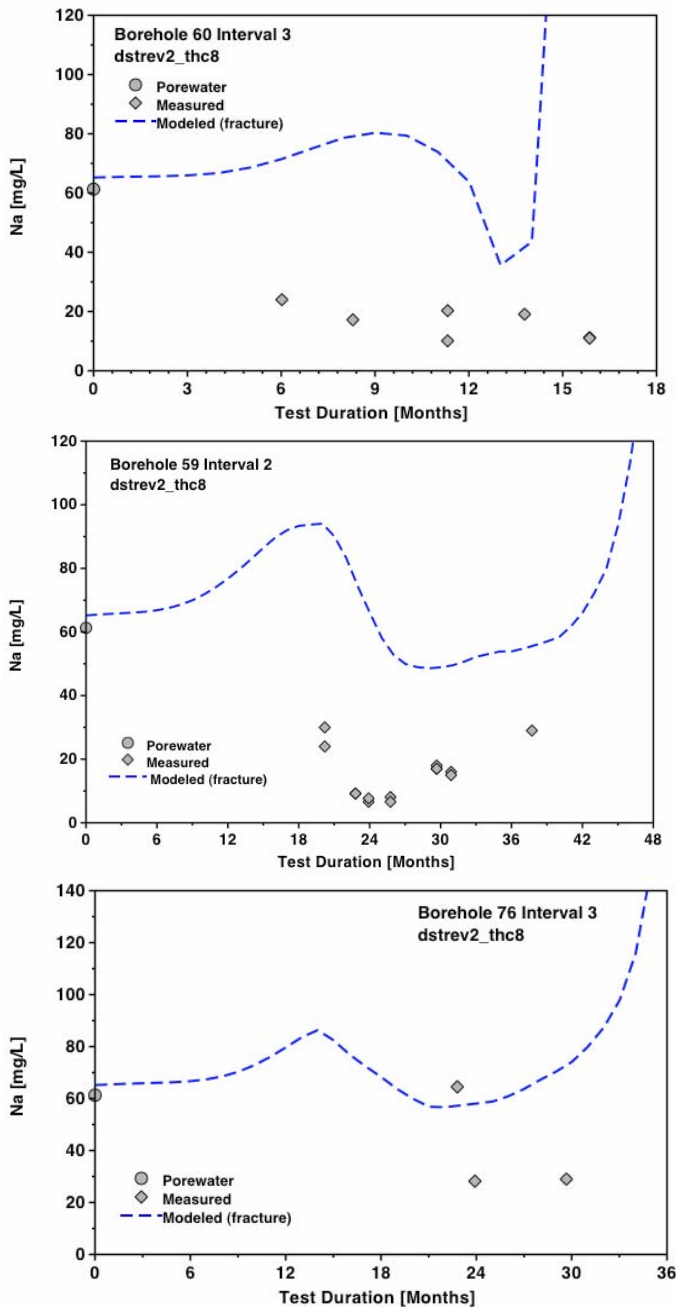


Figure B16.  $\text{Na}^+$  Concentrations (mg/L) in Water Samples Collected from Borehole Intervals (a) 60-3, (b) 59-2, and (c) 76-3 Compared to Modeled  $\text{Na}^+$  Concentrations in Fractures

Calcium is more sensitive to water-rock interaction than some other species because of the fast reaction rate of calcite, its lower solubility with increasing temperature, and the common occurrence of calcite in fractures. Other potential sources of  $\text{Ca}^{2+}$  in the rock include Ca-rich zeolites, such as stellerite that are abundant in fractures. Waters collected from intervals 60-3 and 59-2 show a significant drop from the pore-water concentration (about 100 mg/L) to below 10 mg/L, with a consistent decrease over time in 60-3 (Figure B17). The continued drop in  $\text{Ca}^{2+}$  in 60-3 (Figure B17a) and the very low concentrations in 59-2 (Figure B17b) may be caused by calcite precipitation, because of its decreased solubility with increasing temperature. Modeled  $\text{Ca}^{2+}$  concentrations show a similar trend in Ca reduction but are slightly elevated with respect to the measured values in all the boreholes. The shape of the modeled  $\text{Ca}^{2+}$  curve in 60-3 does not exhibit as early an initial dilution-induced drop in concentration; instead, the reduction occurs later, when the strong condensation pulse is encountered and increasing temperature results in calcite precipitation. The  $\text{Ca}^{2+}$  concentration increases as boiling proceeds and the remaining water is evaporated.

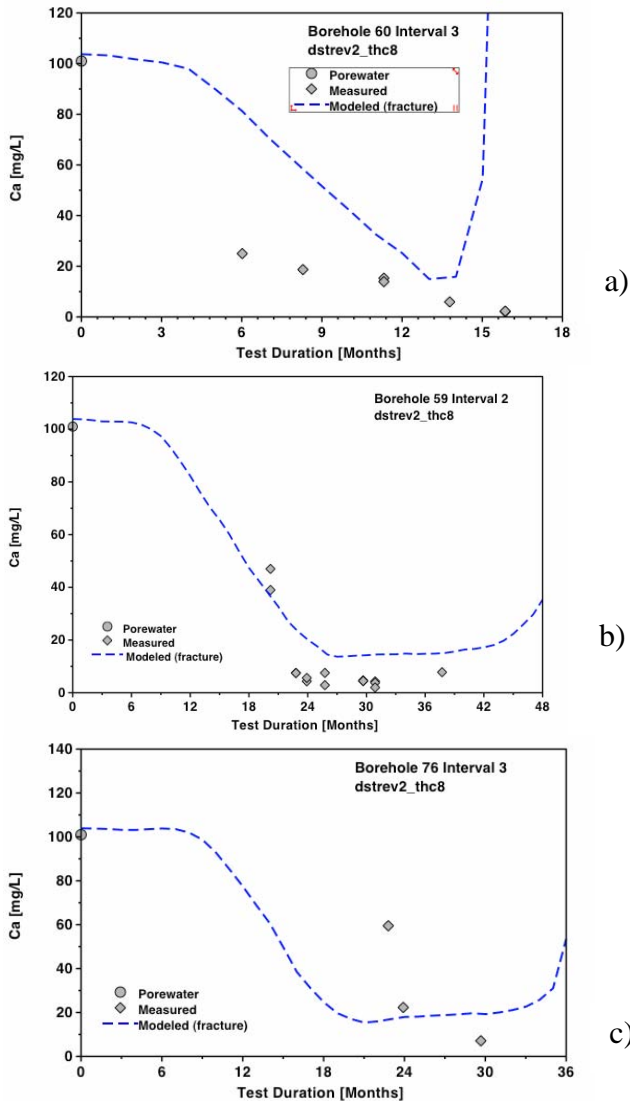


Figure B17.  $\text{Ca}^{2+}$  concentrations (mg/l) in water samples collected from borehole intervals (a) 60-3, (b) 59-2, and (c) 76-3 compared to modeled  $\text{Ca}^{2+}$  in fracture water

Measured silica concentrations (Figure B18) show an increase to significantly higher concentrations in the borehole waters compared to the initial pore-water concentration. The modeled silica concentrations in fracture waters capture the strong increases observed in the measured compositions, especially those seen in the borehole intervals overlying the heaters (59-2 and 76-3). In 76-3, the first water sample collected had a silica concentration of over 280 mg/L, compared to about 180 mg/L in the model simulation. The two waters collected later had silica concentration around 200 mg/L, which was closer to the model results. Because the concentrations of conservative species, such as chloride and sulfate, are close to the measured values, the possibility of greater fracture-matrix interaction is unlikely. Modeled  $\text{Na}^+$  and  $\text{K}^+$  concentrations (see below) also do not deviate substantially from measured values, suggesting that the silica is not likely to have been derived from increased dissolution of feldspars. Thus, the high measured silica concentrations are likely to be a result of dissolution of a silica phase in the fractures (possibly opal-CT) or reaction of “fresh” mineral surfaces (i.e., cristobalite or quartz) in the borehole walls.

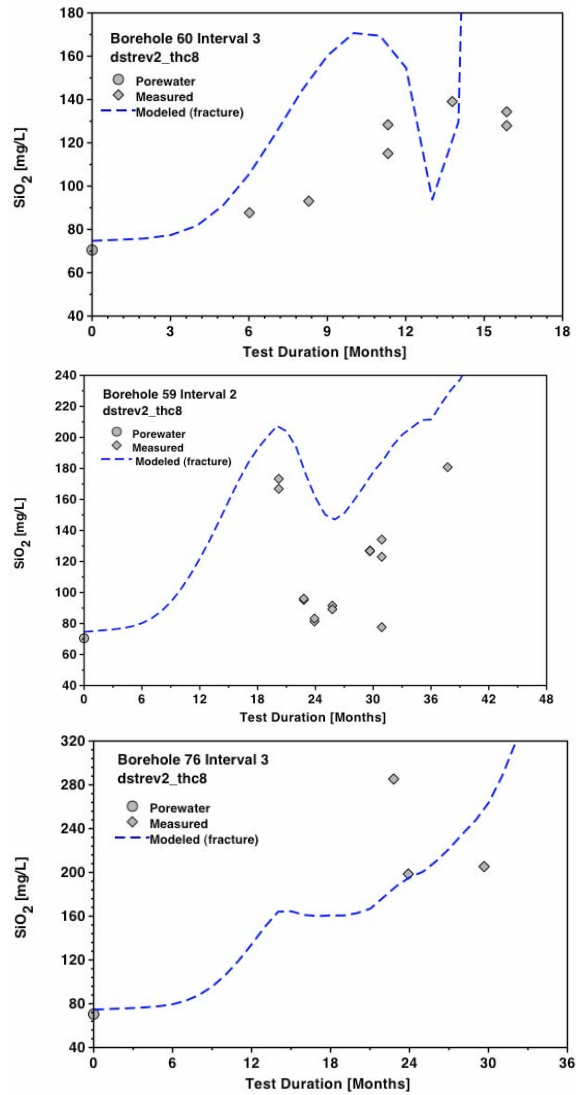


Figure B18.  $\text{SiO}_{2(aq)}$  concentrations (mg/l) in water samples collected from borehole intervals (a) 60-3, (b) 59-2, and (c) 76-3 compared to modeled fracture water  $\text{SiO}_{2(aq)}$  concentrations

Modeled  $K^+$  concentrations (Figure B19), although initially lower, quickly rise during heating and are similar to the measured values. A deviation occurs in  $K^+$  at the initial time, because of some disequilibrium in the initial pore water with the model mineral assemblage. Measured concentrations in waters collected from the boreholes are significantly higher than would be expected from simple dilution of ambient fracture or matrix pore water, indicating that reactions with K-feldspar have likely taken place. Modeled concentrations of  $K^+$ , like those of  $Na^+$ , increase to values somewhat higher than the measured concentrations. However, trends between modeled and measured data are similar, suggesting that a reduction in the K-feldspar reactivity and an increase in the dilution effect would result in a closer match to the measured concentrations. The modifications to hydrological and thermodynamic (and/or kinetic) data required for such reduction in reactivity would be consistent with the shifts needed for both the conservative species, such as  $Cl^-$  and  $SO_4^{2-}$ , as well as for  $Na^+$ . The low matrix permeability induces slower transfer of pore water from the matrix into the fractures, and results in lower dilution of the conservative species. The reactions of calcite and feldspar phases also increase the concentrations of silica, Na and K in the fractures. The fact that  $Na^+$  and  $K^+$  show similar trends over time is consistent with their predominance in either an alkali feldspar solid-solution phase, such as sanidine, and/or as closely intergrown exsolved phases from a precursor solid-solution alkali feldspar mineral.

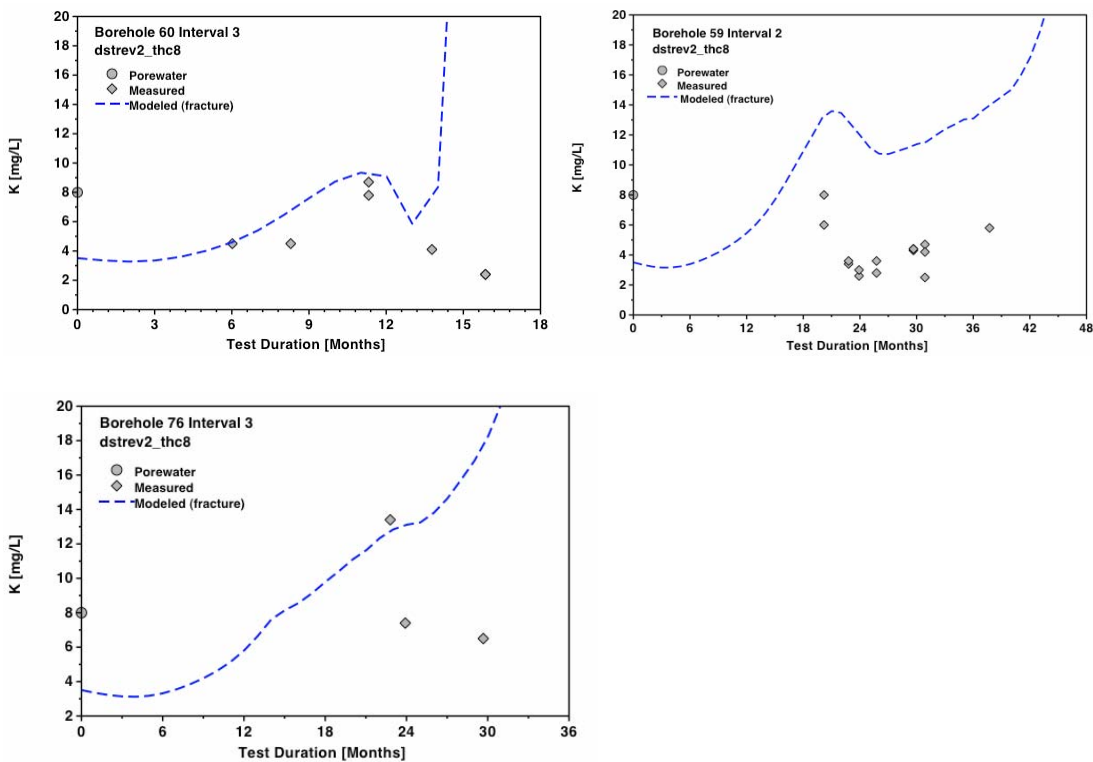


Figure B19.  $K^+$  Concentrations (mg/L) in Water Samples Collected from Borehole Intervals (a) 60-3, (b) 59-2, and (c) 76-3 Compared to Modeled Fracture Water  $K^+$  Concentrations

Few bicarbonate ( $HCO_3^-$ ) concentrations were measured in the borehole waters because of difficulties making the measurements in the field. Available measurements are plotted in Figure B20 compared to the model results. Measured bicarbonate

concentrations are much lower than the initial pore-water concentration, a pattern that is captured well by the model. This trend reflects the combined effects of dilution and loss of dissolved  $\text{CO}_2$  to the vapor phase at higher temperatures.

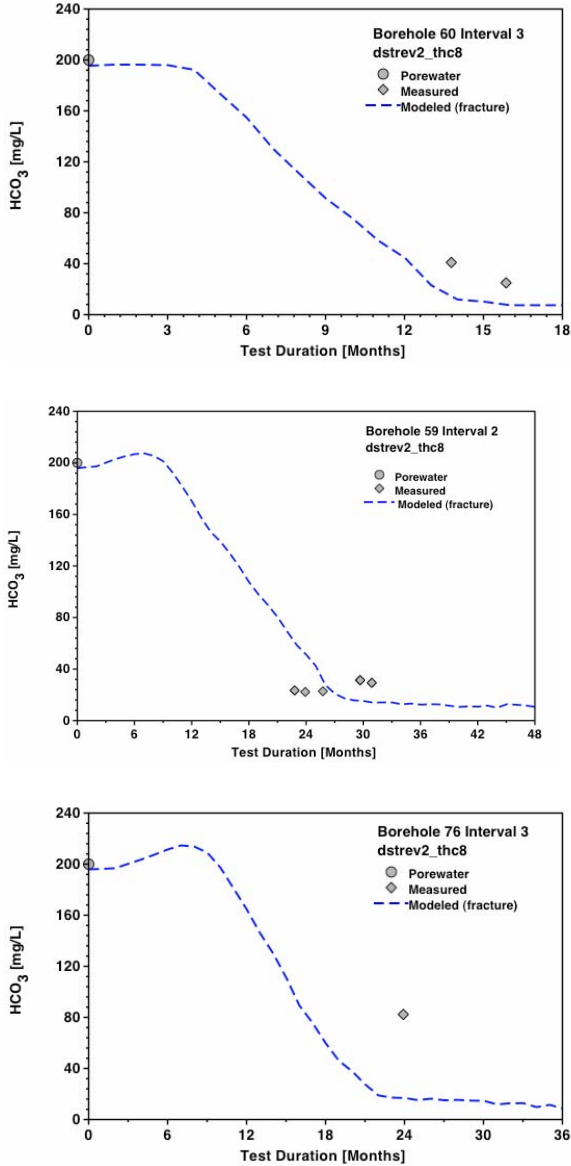


Figure B20.  $\text{HCO}_3^-$  Concentrations (mg/L) in Water Samples Collected from Borehole Intervals (a) 60-3, (b) 59-2, and (c) 76-3 Compared to Modeled Fracture Water  $\text{HCO}_3^-$  Concentrations

Measured  $\text{Mg}^{2+}$  concentrations (Figure B21) show initial concentrations closer to the pore-water value of about 17 mg/L, and then a considerable drop in all the borehole intervals. Modeled  $\text{Mg}^{2+}$  concentrations show a similar pattern and are close to the measured concentrations. The sharp drop in the modeled concentrations is related to a combination of dilution from condensate and the precipitation of sepiolite (a Mg-rich sheet silicate). It is not clear whether precipitation of an Mg-rich phase takes place in the boiling zone in the rock, because the extent of dilution of  $\text{Mg}^{2+}$  is roughly similar to that observed for the conservative species, such as  $\text{Cl}^-$ . Some  $\text{Mg}^{2+}$  is likely

incorporated into calcite that is precipitated as the condensate water above the heaters drains down and boils, although this may have a minimal effect on  $Mg^{2+}$  concentrations. The thermodynamic model for calcite does not include  $Mg^{2+}$ , and therefore, another Mg-bearing phase (i.e., sepiolite) takes up some of the  $Mg^{2+}$ .

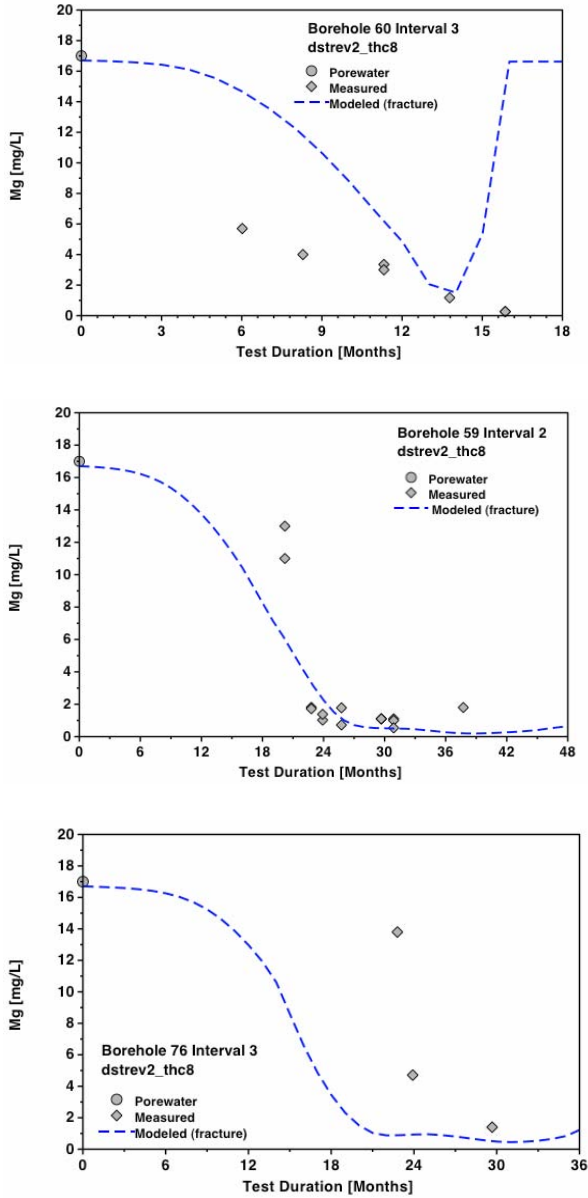


Figure B21.  $Mg^{2+}$  Concentrations (mg/L) in Water Samples Collected from Borehole Intervals (a) 60-3, (b) 59-2, and (c) 76-3 Compared to Modeled Fracture Water  $Mg^{2+}$  Concentrations

Nitrate ( $NO_3^-$ ) is important for the evolution of final salt compositions in potential seepage waters. Nitrate is highly soluble, and there are no nitrate minerals initially present in the tuff. The pore water has somewhat more variable nitrate concentrations compared to  $Cl^-$  and  $SO_4^{2-}$ . The greater variability in pore-water concentrations may be a result of biologically mediated nitrogen reduction, possibly after sample collection. Measured and modeled nitrate concentrations are shown in Figure B22. Concentrations

measured in waters collected from the hydrology boreholes are almost all lower than those from the pore water, showing a similar pattern of depletion as  $\text{Cl}^-$  and  $\text{SO}_4^{2-}$ . This finding suggests that over the time scale of the experiment, nitrate acts as a conservative species and may not have been affected significantly by biological activity in the rock. The modeled concentrations capture the measured pattern of nitrate concentrations quite well, although the dilution effect is not as strong; this effect is similar to that seen for most other weakly reactive or nonreactive species.

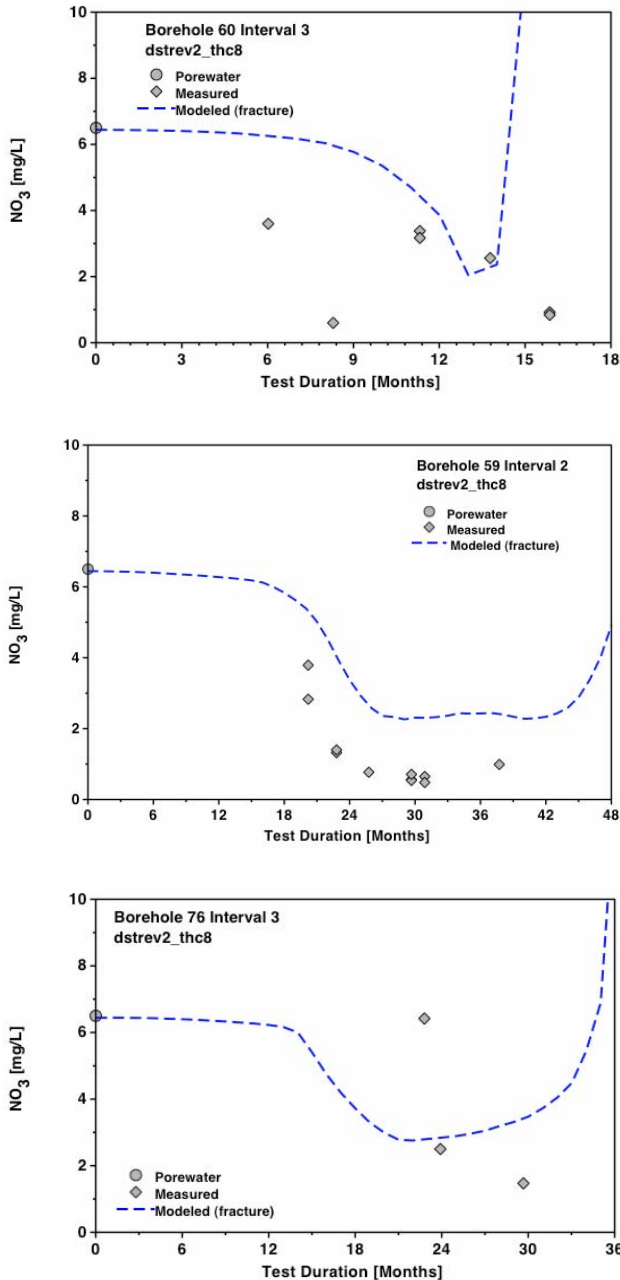


Figure B22.  $\text{NO}_3^-$  Concentrations (mg/L) in Water Samples Collected from Borehole Intervals (a) 60-3, (b) 59-2, and (c) 76-3 Compared to Modeled Fracture Water  $\text{NO}_3^-$  Concentrations

## B5.4 Mineralogical changes

As the last few sections have documented, marked changes have taken place in the water and gas chemistry in the DST, owing to thermal-hydrological processes as well as mineral-water-gas reactions. The total amount of minerals precipitated or dissolved, though, may be exceedingly small, even though the effect on the water composition is quite strong. The strong effect on the water composition is related to the water/rock ratio, which is very low in the unsaturated low-porosity fractured tuff. The system is also characterized by an exceedingly low percolation flux of only a few millimeters per year or less, and therefore the ambient water has a long residence time. This section documents the predicted changes in mineralogy over the heating phase of the DST and compares the results to a few measurements made from *in situ* sidewall core samples obtained from above-boiling zones.

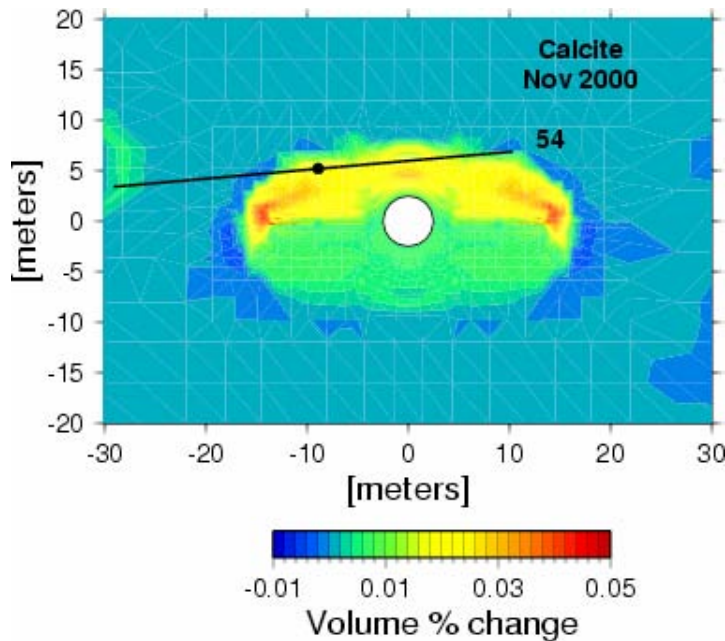
A series of small core samples was analyzed for evidence of mineral alteration during the heating phase of the DST. The first set of samples was obtained in November 2000 by sidewall coring of fractures in “chemistry” boreholes 53 and 54, which were originally designed for water sampling. Because only a small portion of the core has been analyzed and only a few results are available, the comparisons to model results are limited. The data represent observations and analyses from two locations taken about 1 m apart in an above-boiling region above the heaters.

Calcite, amorphous silica, and a calcium sulfate phase (tentatively identified as gypsum) are the only phases in these samples identified so far as products of the processes taking place during the DST. Amorphous silica was common in both samples, whereas calcite and gypsum were only described from the sample further into the above-boiling zone (the other sample was from the outer edge). Although anhydrite is thermodynamically more stable than gypsum under the conditions of the DST, gypsum was observed in analyses of borehole surfaces from the Single Heater Test. On the basis of this identification, the calcium sulfate phase observed in the DST sidewall core samples was considered to be gypsum (BSC 2002a).

From these descriptions, amorphous silica was the dominant phase precipitated during boiling, with much lesser amounts of calcite and gypsum. Amorphous silica appears as glassy coatings covering larger areas of the surface, commonly in the form of thin curled sheets and fine tubules. Calcite typically is found as scattered, small late-stage mounds, with gypsum as very late-formed scattered crystals on top of other phases. The actual percentage of mineral precipitates in the fracture system could not be determined from this type of localized analysis. Some of the silica coatings were approximately 10–20  $\mu\text{m}$  thick, with discrete gypsum crystals up to 80  $\mu\text{m}$  long. Given a uniform 10  $\mu\text{m}$  thick layer of mineral precipitates on one side of all fractures, with a hypothetical range in fracture aperture of 100 to 1,000  $\mu\text{m}$ , the proportion of fracture volume filled would range from 1 to 10%. Because many of the coatings are much less than 10  $\mu\text{m}$  thick and do not cover all areas of every fracture, the volume filled is likely to be less than 1%.

Although calcite is not a major phase in the tuffs at Yucca Mountain, its rapid reaction rate, pH sensitivity, strong effect on pH, and presence almost entirely in fracture coatings make it an important mineral phase. Predicted changes in calcite volume percent in fractures after approximately three years of heating are shown in Figure B23. The simulated changes in calcite abundances show a well-defined region of precipitation in the fractures above and to the margins of the Heated Drift and wing heaters. Strong dissolution is evident below the wing heaters, especially in the drainage zones. Precipitation in the matrix is driven mainly by increasing temperature and pH, whereas in the fractures there is continuous boiling of condensate waters as they drain

back to the heat source from the overlying condensation zone. These waters pick up  $\text{Ca}^{2+}$  through interaction with calcite and from mixing of ambient fracture pore water. The continuous process of condensate formation and drainage leads to a well-defined zone of calcite precipitation in the fractures above the heaters. The results are also consistent with the decrease in  $\text{Ca}^{2+}$  seen in the condensate waters over time (Figure B17). The predicted location of calcite precipitation also matches the location of observed calcite in the sidewall core sample.



NOTE: Chemistry borehole 54 is shown, with location of observed calcite (filled circle) formed during the DST.

Figure B23. Modeled volume percent change in calcite in fractures as of November 2000 (35 months of heating)

Areas of modeled amorphous silica precipitation are shown in Figure B24. Like calcite, amorphous silica precipitation is concentrated in the reflux zones above the heaters. However, because silica phases have increased solubility at higher temperatures, the zone of amorphous silica precipitation is confined to regions where the temperatures are at or above boiling and evaporation was the primary mechanism for mineral precipitation. The maximum amount of amorphous silica precipitated is about 0.4% after 3 years and less than about 1% for the entire duration of the DST. Although the volumetric percentage of amorphous silica that has precipitated is small, the greatest amount of precipitation occurs at the outer edge of the wing heaters (where flow is focused into boiling regions). There is also an excellent correspondence in the region of modeled amorphous silica precipitation and the observed amorphous silica in the sidewall core samples from borehole 54. Although the observations of mineral coatings on a few samples cannot be used to judge the total amount of mineral precipitated, the small volumes precipitated in the model are consistent with the generally thin coatings observed.

Precipitation of gypsum is localized to the zones where modeled sulfate concentrations become very high as a result of boiling (Figure B25). The observed

location of gypsum in the sidewall core sample is consistent with the model results, which show this sample to be just within the edge of the modeled zone of precipitation. Further sampling through the center of the boiling zone should help delineate the pattern of mineral precipitation for all the phases.

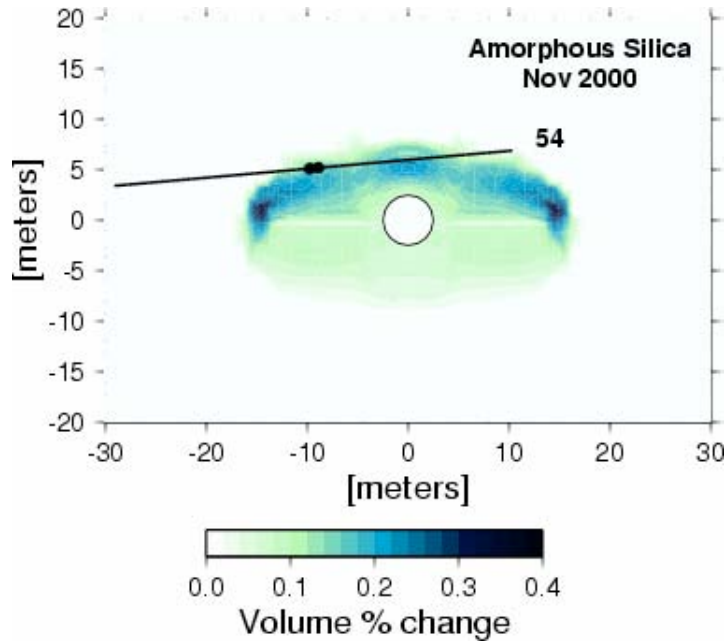


Figure B24. Modeled volume percent amorphous silica in fractures as of November 2000 (35 months of heating). NOTE: Chemistry borehole 54 is shown, with location of observed amorphous silica (filled circle) formed during the DST.

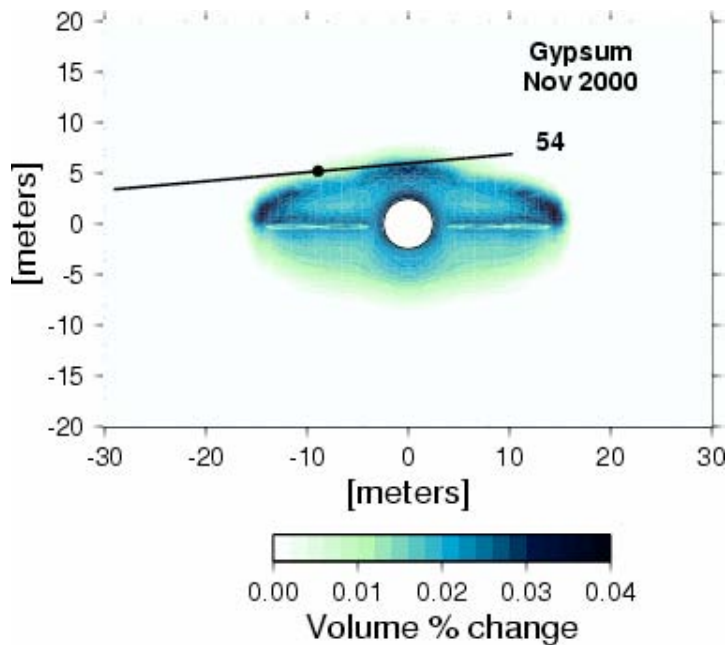


Figure B25. Modeled volume percent gypsum in Fractures as of November 2000 (35 months of heating). NOTE: Chemistry borehole 54 is shown, with location of observed gypsum (filled circle) formed during the DST.

The observation of significantly greater amorphous silica precipitation compared to calcite and gypsum, with the latter phases occurring in roughly equivalent amounts, is consistent model results. Although the predicted maximum amount of amorphous silica precipitated is about an order of magnitude greater than calcite, there are not enough samples to determine the spatial distribution of these phases and whether areas exist where the relative proportions differ. Additional boreholes have been drilled through the boiling zone to examine the distribution of mineral alteration and the effects on matrix pore-water composition. These boreholes will allow for a systematic examination of fracture mineral alteration away from the localized TH effects induced by open boreholes.

### B5.5 Porosity and permeability changes

Figure B26 shows the change in fracture porosity after 4 years of heating in the DST. The areas above the Heated Drift and near the edges of the wing heaters show the greatest reduction in fracture porosity, reaching somewhat less than -0.8%. Areas of slight fracture porosity increases in the model results can be found in the outer condensation zones, yet they are not evident in the contour plot. Changes in matrix porosity (not shown), are approximately two orders of magnitude less than the modeled changes in the fractures.

Fracture permeability changes resulting from mineral precipitation and dissolution are tied to changes in porosity and more directly to fracture aperture changes. Changes in fracture porosity of less than 1% of the original value would have a correspondingly small effect on fracture permeability. These results are consistent with the observations of relatively small reductions in air permeability during the DST, which have been attributed predominantly to water saturation changes and mechanical effects.

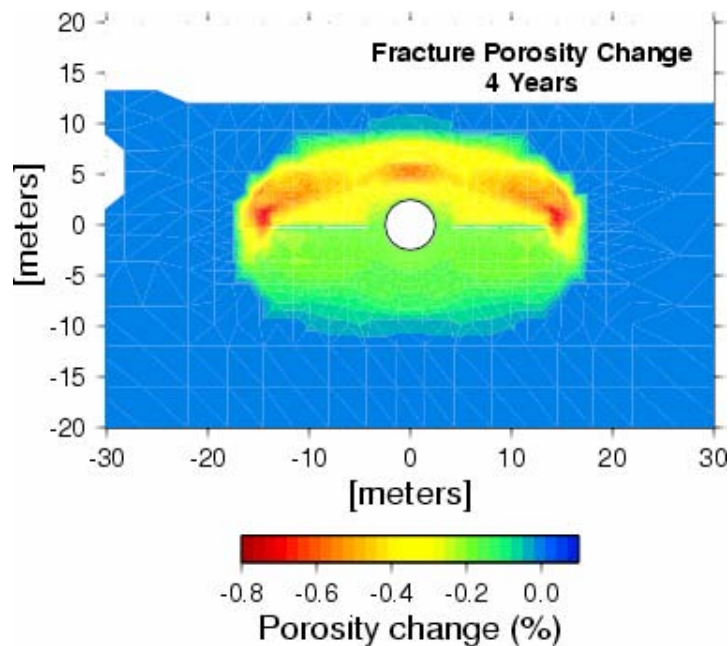


Figure B26. Change in fracture porosity after four years of heating. NOTE: Negative values indicate a net porosity reduction resulting from mineral precipitation, and positive values indicate a net porosity increase resulting from mineral dissolution.

## B6. Concluding remarks

A 2-D dual permeability model for coupled thermal, hydrological, and chemical processes in the Drift Scale Test has been presented, with comparisons to measured geochemical data over the 4 year heating phase. The model considers the flow of heat, liquid and gas, transport of aqueous and gaseous species by diffusion and advection, and local kinetic and equilibrium reactions between minerals, aqueous fluid, and gas. The thermal-hydrological model includes a detailed history of power input to heaters and times of power reductions and losses.

Comparisons of modeled concentrations and the chemistry of water (e.g., pH,  $\text{SiO}_2(\text{aq})$ ,  $\text{Na}^+$ ,  $\text{K}^+$ ) and gas samples ( $\text{CO}_2$ ) collected from boreholes over the heating phase show that the THC model captures the trends and magnitude of chemical changes. In particular,  $\text{CO}_2$  concentrations in gas samples increase from an initial value of about 1000 ppmv to greater than 25,000 ppmv as a result of exsolution from matrix pore water and transport into fractures. The  $\text{CO}_2$  dissolves into condensate waters at lower temperatures, resulting in a drop in pH and also dissolution of calcite.

Some of the processes that could explain the water chemistry of samples collected in the hydrology boreholes include mixing of pure condensate water with fracture pore waters, equilibration of condensate waters with matrix pore waters via molecular diffusion, reactions of condensate waters with fracture-lining minerals, and mineral precipitation. Some clear trends in water chemistry of the condensate waters over time are increases in pH and  $\text{SiO}_2(\text{aq})$  concentration and a drop in  $\text{Ca}^{2+}$ . The higher silica concentration in the waters collected at later times in several boreholes (and at higher temperatures), relative to chloride and the initial pore-water silica concentration, is consistent with dissolution of a silicate phase, rather than with increased concentration via boiling. Concentrations of  $\text{K}^+$ ,  $\text{Mg}^{2+}$ , and  $\text{Na}^+$  are also higher than what would be expected by dilution of original pore water (as evidenced by the low chloride concentrations). Therefore, the silicate phases that dissolved must have been some combination of silica polymorphs (i.e., opal, cristobalite, tridymite, and quartz) and feldspar, clays, or zeolites, rather than just a pure silica phase. Many of the waters show a drop in  $\text{Ca}^{2+}$  over time, consistent with calcite precipitation as the water was heated further and underwent  $\text{CO}_2$  degassing.

A precipitation zone of secondary mineral phases such as amorphous silica, calcite, and gypsum in fractures has also been successfully predicted in a narrow reflux zone above the heaters. Consistent with the observation of coatings of amorphous silica that are tens of microns or less in thickness, the predicted fracture porosity change is less than one percent.

Because the chemical changes are so closely tied to the TH processes and fracture-matrix interaction, modeling several chemical components provides an independent method for validating and refining TH models (e.g., the "Active Fracture Model" for fracture-matrix interaction and the dual-permeability method). Based on the strong dilution trends of non-reactive species, such as chloride and sulfate, the extent of interaction of fracture condensate water with matrix pore water may have been limited. However, effects of the interaction of dilute fracture waters on matrix pore waters are just now being investigated and future studies will allow for a more quantitative assessment of the extent of fracture-matrix interaction

## Acknowledgements

Aqueous geochemical data from the Drift Scale Test were obtained by Laura DeLoach (Lawrence Livermore National Lab). Schon Levy (Los Alamos National Lab) determined the mineral abundances in fractures. Sumit Mukhopadhyay and Jens Birkholzer developed the initial TH grid from which the THC model was developed. John Apps and Sonia Salah worked on the thermodynamic and kinetic databases. This work was supported by the Director, Office of Civilian Radioactive Waste Management, U.S. Department of Energy, through Memorandum Purchase Order EA9013MC5X between Bechtel SAIC Company, LLC, and the Ernest Orlando Lawrence Berkeley National Laboratory (Berkeley Lab). The support is provided to Berkeley Lab through the U.S. Department of Energy Contract No. DE-AC03-76SF00098.

## References

- BSC (Bechtel SAIC Company). *Thermal Testing Measurements Report*. Las Vegas, Nevada: Bechtel SAIC Company. 2002a.
- BSC (Bechtel SAIC Company). *Users Manual (UM) for TOUGHREACT V3.0*. 10396-UM-3.0-00. Las Vegas, Nevada: Bechtel SAIC Company. 2002b.
- CRWMS M&O (Civilian Radioactive Waste Management System Management and Operating Contractor). *Drift Scale Test As-Built Report*. Las Vegas, Nevada: CRWMS M&O. 1998.
- Bear, J. *Dynamics of Fluids in Porous Media*. New York, New York: Dover Publications. 1998.
- Birkholzer, J.T. and Y.W. Tsang. *Pretest Analysis of the Thermal-Hydrological Conditions of the ESF Drift Scale Test*. Yucca Mountain Project Level 4 Milestone SP9322M4. Berkeley, California: Lawrence Berkeley National Laboratory. 1997.
- Birkholzer, J. T. & Tsang, Y. W. *Interpretive Analysis of the Thermo-Hydrological Processes of the Drift Scale Test*. In: Drift Scale Test Progress Report, Chapter 6. Yucca Mountain Project Level 4 Milestone SP2930M4. Berkeley, California: Lawrence Berkeley National Laboratory. 1998.
- Carroll, S.; Mroczek, E.; Alai, M.; and Ebert, M. *Amorphous Silica Precipitation (60 to 120°C): Comparison of Laboratory and Field Rates*. *Geochimica et Cosmochimica Acta*, 62, (8), 1379-1396. 1998.
- Ehrlich, R.; Etris, E.L.; Brumfield, D.; Yuan, L.P.; and Crabtree, S.J. *Petrography and Reservoir Physics III: Physical Models for Permeability and Formation Factor*. AAPG Bulletin, 75, (10), 1579-1592. 1991.
- Helgeson, H.C.; Kirkham, D.H.; and Flowers, G.C. *Theoretical Prediction of the Thermodynamic Behavior of Aqueous Electrolytes at High Pressures and Temperatures: IV. Calculation of Activity Coefficients, Osmotic Coefficients, and Apparent Molal and Standard and Relative Partial Molal Properties to 600°C and 5 kb*. *American Journal of Science*, 281, (10), 1249-1516. 1981.
- Langmuir, D. *Aqueous Environmental Geochemistry*. Upper Saddle River, New Jersey: Prentice Hall. 1997.
- Lasaga, A.C. *Kinetic Theory in the Earth Sciences*. Princeton, New Jersey: Princeton University Press. 1998.
- Lide, D.R. (ed.). *CRC Handbook of Chemistry and Physics*. 74th Edition. Boca Raton, Florida: CRC Press. 1993.

- Liu, H.H., Doughty, C., & Bodvarsson, G.S. *An active fracture model for unsaturated flow and transport in fractured rocks*. *Water Resources Research*, 34(10), 2633–2646. 1998.
- Reed, M.H. *Calculation of Multicomponent Chemical Equilibria and Reaction Processes in Systems Involving Minerals, Gases and an Aqueous Phase*. *Geochimica et Cosmochimica Acta*, 46, (4), 513-528. 1982.
- Rimstidt, J.D. and Barnes, H.L. *The Kinetics of Silica–Water Reactions*. *Geochimica et Cosmochimica Acta*, 44, 1683-1699. 1980.
- Slider, H.C. *Practical Petroleum Reservoir Engineering Methods, An Energy Conservation Science*. Tulsa, Oklahoma: Petroleum Publishing Company. 1976.
- Sonnenthal E. and N. Spycher. *Drift-Scale Coupled Processes (Drift-Scale Test and THC Seepage) Models*. REV01. Lawrence Berkeley National Laboratory, Berkeley, CA. 2001.
- Sonnenthal, E. and N. Spycher. *Drift Scale Coupled Processes (Drift Scale Test and THC Seepage) Models*. REV00. Lawrence Berkeley National Laboratory, Berkeley, CA. 2000.
- Sonnenthal, E., N. Spycher, and J. Apps. Interpretative analysis of the thermo-hydro-chemical processes of the Drift Scale Test, Chapter 3. In: Tsang, Y., J.T. Birkholzer, E.L. Sonnenthal, N. Spycher, J. Apps, J. Peterson, and K. Williams. *Yucca Mountain Drift Scale Test Progress Report*, LBNL-42538, p. 3-1 - 3-56. 1999.
- Sonnenthal, E., N. Spycher, J. Apps, and A. Simmons. *Thermo-hydro-chemical predictive analysis for the Drift-Scale Heater Test*. Level 4 Milestone SPY289M4. Lawrence Berkeley National Laboratory. 1998.
- Spycher, N., E. Sonnenthal, P. Dobson, J. Apps, John, S. Salah, T. Kneafsey, and C. Haukwa. *Drift-Scale Coupled Processes (DST and THC Seepage) Models*, REV02. Lawrence Berkeley National Laboratory, Berkeley, CA. 2003.
- Steeffel, C.I. and Lasaga, A.C. *A Coupled Model for Transport of Multiple Chemical Species and Kinetic Precipitation/Dissolution Reactions with Application to Reactive Flow in Single Phase Hydrothermal Systems*. *American Journal of Science*, 294, (5), 529-592. 1994.
- Xu, T., & Pruess, K. *Modeling multiphase non-isothermal fluid flow and reactive geochemical transport in variably saturated fractured rocks: 1. Methodology*. *American Journal of Science*, 301: pp. 16-33. 2001.
- Xu T., Sonnenthal, E., Spycher, N., Pruess, K., Brimhall, G., & Apps, J. *Modeling multiphase non-isothermal fluid flow and reactive geochemical transport in variably saturated fractured rocks: 2. Applications to supergene copper enrichment and hydrothermal flows*. *American Journal of Science*, 301: pp. 34-59. 2001.
- Xu, T., Sonnenthal, E., Spycher, N., & Pruess, K. *TOUGHREACT: A new code of the TOUGH family of non-isothermal multiphase reactive geochemical transport in variably saturated media*. *Proceedings, TOUGH Symposium*, 2003.



[www.ski.se](http://www.ski.se)

**STATENS KÄRNKRAFTINSPEKTION**  
Swedish Nuclear Power Inspectorate

**POST/POSTAL ADDRESS** SE-106 58 Stockholm

**BESÖK/OFFICE** Klarabergsviadukten 90

**TELEFON/TELEPHONE** +46 (0)8 698 84 00

**TELEFAX** +46 (0)8 661 90 86

**E-POST/E-MAIL** [ski@ski.se](mailto:ski@ski.se)

**WEBBPLATS/WEB SITE** [www.ski.se](http://www.ski.se)